iScience

CellPress
OPEN ACCESS

Article

Kinetic Separation of Oxidative and Non-oxidative Metabolism in Single Phagosomes from Alveolar Macrophages: Impact on Bacterial Killing

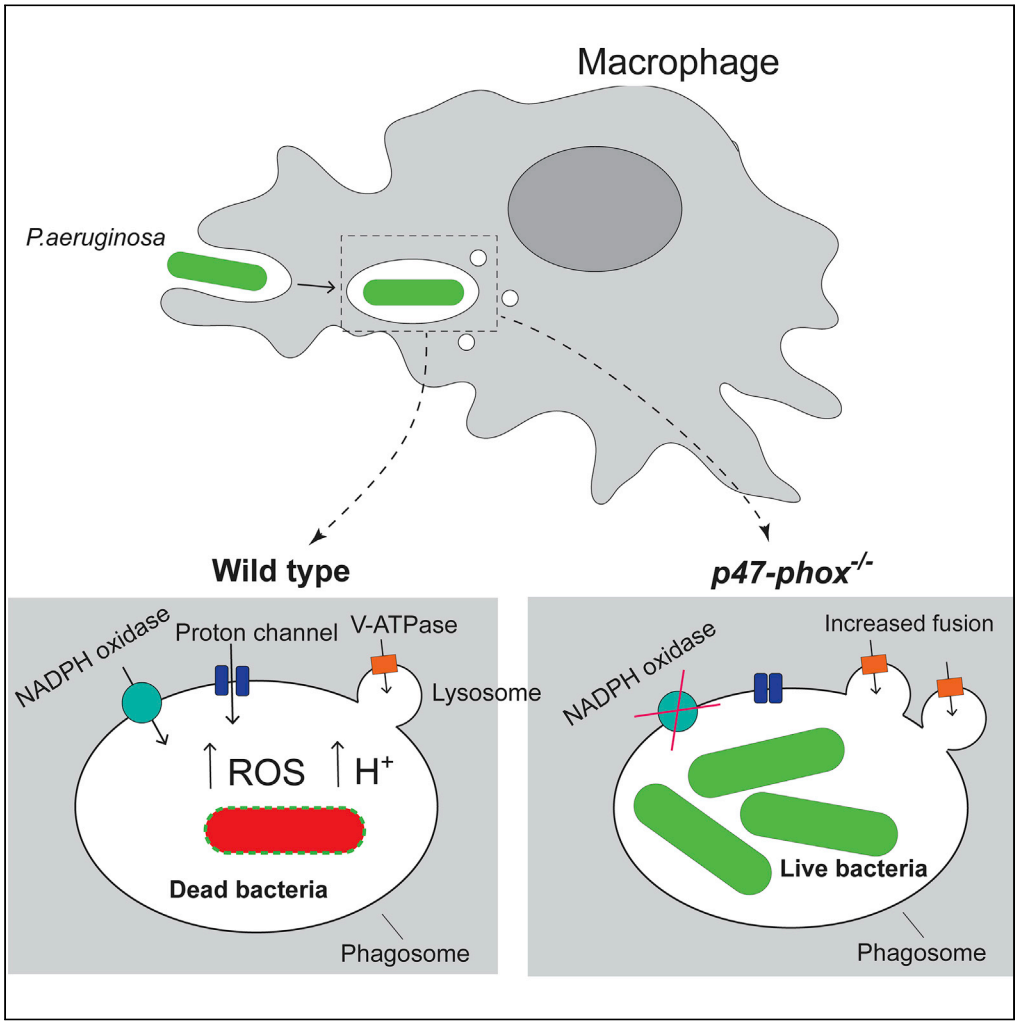

Vladimir Riazanski,
Zihao Sui,
Deborah J. Nelson

vryazanskiy@uchicago.edu (V.R.)
nelson@uchicago.edu (D.J.N.)

HIGHLIGHTS

Phagosomal NOX and V-ATPase activation is sequential and separable in macrophages

Superoxide (O_2^-) inhibits lysosomal fusion thereby inhibiting phagosomal acidification

Phagosomes in single cells are heterogeneous in NOX activity and thereby acidification

NOX activity is the dominant factor in bactericidal efficacy in macrophage phagosomes

Riazanski et al., iScience *23*, 101759
November 20, 2020
https://doi.org/10.1016/j.isci.2020.101759

iScience

CellPress
OPEN ACCESS

Article

Kinetic Separation of Oxidative and Non-oxidative Metabolism in Single Phagosomes from Alveolar Macrophages: Impact on Bacterial Killing

Vladimir Riazanski,[1,*] Zihao Sui,[1] and Deborah J. Nelson[1,2,*]

SUMMARY

The relative contribution of the two phagosomal catabolic processes, oxidative and metabolic, was assessed in the killing of *Pseudomonas aeruginosa* in phagosomes of alveolar macrophages (AMs) from wild-type (*p47-phox*$^{+/+}$) or NOX-defective (*p47-phox*$^{-/-}$) mice. Free radical release and degradative acidification within AM phagosomes is sequential and separable. The initial NOX activity, identifiable as a transient alkalinization, leads to fast bacterial wall permeabilization by ROS. This is followed by V-ATPase-induced acidification and enzymatic bacterial degradation contributed through phagosomal-lysosomal fusion. The alkalinization/acidification ratio was variable among phagosomes within single cells of a given genotype and not as a function of macrophage M1 or M2 classification, possibly owing to uneven distribution of phagosomal transporter proteins. Irregular, excessive NOX activity prevents phago-lysosomal fusion, and the lack of V-ATPase-induced acidification leads to bacterial stasis in the phagosome. Thus, efficient phagosomal bacterial killing is a result of tightly balanced activity between two processes.

INTRODUCTION

As an intracellular organellar population unique to professional phagocytes in the innate immune system and dedicated to microbicidal function, phagosomes carry out their task in a highly divergent manner depending upon cellular context and ion transporter expression. In their role as sentinels against pathogenic invasion, macrophages differ dramatically in their mechanistic approach to bacterial processing from their phagocytic cousin, the neutrophils. Circulating neutrophils utilize, almost exclusively, oxidative metabolism to kill bacteria. Membrane bound NADPH oxidase (NOX) generates superoxide anion (O_2^-), which is released into the nascent phagosomal lumen obligating charge buffering through a proton influx into the cargo-loaded compartment (Nunes et al., 2013).

Tissue macrophages produce 10- to 20-fold less O_2^- than that produced by neutrophils (Piacenza et al., 2019). Instead, the phagosomes of tissue macrophages utilize two catabolic pathways in bacterial killing. Macrophages use the oxidative pathway, or respiratory burst, present in neutrophils, but it is transient and attenuated in macrophage phagosomes. The production of O_2^- is followed by enzymatically driven bacterial degradation. The degradative process is initiated by phagosomal fusion with lysosomes and endo-lysosomes contributing a spectrum of catabolic enzymes that require an acidic environment for their activity. The acidity of the macrophage phagosome is generated by the activity of the vesicular ATPase (V-ATPase), donated by endo-lysosomal compartment fusion, a process that requires an anion charge compensation through a Cl^- selective influx into, or cation efflux from, the phagosome. Phagosomal acidification has a direct bactericidal or bacteriostatic effect as bacterial growth is inhibited, in general, at low pH. In addition to the acidic activation of bacterial degradative lipases and proteases contributed by lysosomes, acidification promotes the dismutation of O_2^- to hydrogen peroxide (H_2O_2), itself a potent microbicidal agent. An extensive and recent comparative analysis of the phagosomal pH within cells of the phagocytic lineage—neutrophils, monocytes, dendritic cells, and monocyte derived cells—has revealed a surprising heterogeneity with respect to differentiation stimuli (Foote et al., 2019) and the suggestion that phagosomal pH might also be a function of cargo.

Considering that phagosomes in tissue macrophages utilize the two catabolic pathways in bacterial killing—oxidative and non-oxidative—we set out to determine if the two pathways were separable by their time-dependent activation following cargo uptake and whether they could interact with each other and

[1]The University of Chicago, Department of Pharmacological and Physiological Sciences, 947 E. 58th Street, MC 0926, Chicago, IL 60637, USA

[2]Lead Contact

*Correspondence: vryazanskiy@uchicago.edu (V.R.), nelson@uchicago.edu (D.J.N.)

https://doi.org/10.1016/j.isci.2020.101759

both contribute to bactericidal activity. More importantly, however, we asked the question of dominance: in the phagocytic arsenal, which process controls the balance between killing and survival of the captured pathogen? We carried out these experiments using *in vivo* live cell microscopy to follow directly phagosomal pH kinetics and cargo viability, as surrogates for the two catabolic pathways.

The two electrogenic catabolic pathways mirror one another in their requirement for channel-mediated ion influx into the phagosomal lumen. In the case of NOX activation, protons are used as a charge shunt to accompany O_2^- production and further reactive oxygen species generation. In the case of V-ATPase-mediated acidification, Cl^- anions accompany proton transport. Oxidative metabolism generates a phagosomal lumen that is neutral, or transiently alkalotic, presumably owing to enhanced proton consumption during dismutation of O_2^- into H_2O_2 (Jankowski et al., 2002). The fact that neutrophil phagosomes maintain a neutral pH, following cargo uptake, suggests that O_2^- generation and proton flux through the ion channel, Hv1, are well matched (Murphy and DeCoursey, 2006) (DeCoursey, 2016). We reasoned that non-oxidative metabolism is likely to be a slower process, because it requires phagosomal organellar fusion, subsequent acquisition of transport proteins, and sequelae that include the development of an acidic phagosomal compartment (Flannagan et al., 2012). The time required for macrophage phagosomal luminal pH to become acidic is equally well documented, suggesting that the anion charge shunt lags behind V-ATPase activity (Riazanski et al., 2015) (Canton et al., 2014). The binary impact on phagosomal luminal pH, which characterized the two phagosomal catabolic pathways, formed our initial observation that oxidative and non-oxidative metabolism might be separable kinetically in the tissue macrophage.

Tissue macrophage transport proteins that control phagosomal function are derived from both plasma membrane and endo-lysosomal sources during cargo uptake and organellar maturation. Binding of pathogen or an inert particle to the cellular surface is mediated by an array of receptors, including FcR and Toll-like receptors, that signal cellular responses (Flannagan et al., 2012). Ion channels, as well as oxidase subunits, are taken up as components of the plasma membrane that eventually encompasses the captured cargo. These transport proteins reflect the plasma membrane expression profile of the specific tissue macrophage and are a contributing element to macrophage phagosomal heterogeneity between macrophage tissue sources and even between phagosomes within the same cell. Thus, the contribution of the two catabolic pathways may depend upon the density of a given ion channel or transport protein acquired in the formation of the phagosome during particle uptake. Selective subpopulations of macrophages, recently identified as M1 and M2, and defined by predominant presence of either oxidative or non-oxidative pathway, may simply reflect differential transport protein expression during differentiation in culture and not a genetic divergence of macrophage subpopulations *in vivo* (Flannagan et al., 2012).

Using high-resolution, live cell imaging of murine, alveolar macrophage phagosomes, we have traced the activation kinetics of phagosomal oxidative and non-oxidative metabolism *in situ*, following zymosan, as well as *Pseudomonas aeruginosa* uptake. Our data suggest that the initial transient oxidative burst serves to rapidly permeabilize the cell wall of the phagocytosed pathogen, as evidenced by propidium iodide (PI) uptake, whereas the slower developing, enzymatically driven non-oxidative pathway provides the final step in pathogen degradation, rendering the bacterial killing irreversible.

RESULTS

Identification of the Oxidative and Non-oxidative Catabolic Pathways

Initial insights into the process of bacterial killing in macrophages came from classical propidium iodide (PI) experiments carried out at high resolution in live cell confocal microscopy as illustrated in Figure 1. In order to minimize phototoxic damage in AMs, long-term time-lapse imaging of bacterial phagocytosis by AMs was done combining DIC and fluorescent imaging that allowed tracking of fluorescent bacteria relative to individual AMs with minimal cellular damage. At the end of each experiment, AMs were loaded with the fluorescent dye CellTracker Deep Red in order to outline AM surfaces for analysis with Imaris software. Images were rendered in a three-dimensional format, enabling the internalized bacteria to be differentiated from those remaining on the outside or outer surface. Using this technique, we were able to observe and differentiate adherent versus internalized bacteria with a compromised cell membrane as they take up PI that fluoresces red following reversible interaction with internal DNA as seen in Figures 2A and 2D. Isolated murine alveolar macrophages (AMs) were exposed to EGFP-expressing *P. aeruginosa* in the presence of 60 μM PI. The time course of the appearance of PI fluorescence in phagocytosed bacteria is documented

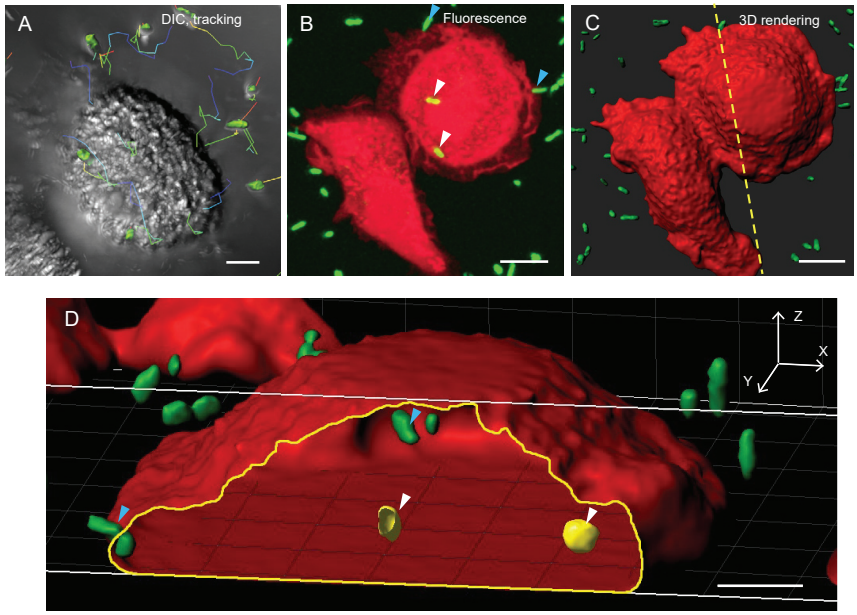

Figure 1. Tracking of Bacterial Phagocytosis by Alveolar Macrophages

(A) A representative composite image (gray, DIC; green, EGFP) of an Imaris tracking over time of EGFP expressing *P. aeruginosa* (shown in rendered form with colored tracking "tail" lines) and an AM in DIC (scale bar, 5μm).

(B) A composite fluorescent image of two adjacent AMs loaded with fluorescent dye CellTracker Deep Red (red) and EGFP expressing *P. aeruginosa* (green). White arrows point to internalized bacteria, blue arrows to entering AMs bacteria.

(C) The same image shown in (B) after 3D rendering in Imaris software. Yellow dotted line shows direction of a crosscut shown in (D) (scale bar 10 μm).

(D) The crosscut of a 3D rendered AM (red, shown in A–C) shows rendered bacteria outside of the cell (green), bacteria entering AM (pointed with blue arrows), and internalized bacteria (pointed with white arrows) (scale bar, 5 μm).

in Figure 2C. Bacterial PI uptake, a result of membrane damage in the captured *P. aeruginosa,* occurred within 5 min after the initiation of phagocytosis (see Video S1). Inhibition of the oxidative pathway in AMs isolated from mice defective in NOX activity (*p47-phox*$^{-/-}$) or in littermate wild-type (*p47-phox*$^{+/+}$) AMs treated with the oxidase inhibitor, diphenyleneiodonium chloride (DPI, 10 μM), resulted in a significant decrease in the percentage of bacteria taking up PI in phagosomes (Figure 2B). Inhibition of the non-oxidative pathway in cells with the V-ATPase inhibitor, bafilomycin (BAF, 1 μM), did not change the percentage of bacteria in phagosomes taking up PI over that observed in control phagosomes (Figure 2B), indicating that the initial uptake of PI was not due to an acidic enzymatic digestion of bacterial membrane. Interestingly, the time course of PI uptake was inversely correlated with the loss of bacterial GFP fluorescence (Figure 2C), perhaps signaling the onset of phagosomal acidification and enzymatic digestion in phagosomes, both of which could result in EGFP fluorescence quenching. In order to determine whether the quenching of EGFP corresponds to the summed response to both acidic pH and degradation we compared kinetic responses to changes in both PI and EGFP fluorescence in the presence and absence of BAF (1μM) (see Figure S1). Quenching in the absence of V-ATPase activity is reduced in the presence of BAF, but it is not absent. Data from this experiment allowed us to conclude that the loss of EGFP fluorescence with time is due to the contribution of both the development of an acidic phagosomal lumen and resultant degradation. An alternative explanation might be put forward postulating that permeabilization of bacterial membranes precedes phagosomal sealing and, therefore, a fraction of cytoplasmic bacterial EGFP might be lost to the extracellular milieu. Our results cannot rule out this possibility.

Phagosomal bacterial morphology, observed at a higher resolution, revealed that a sequential loss of bacterial EGFP fluorescence, followed by loss of bacterial rod shape, correlated with an increase in PI intensity (Figure 2D). The most parsimonious conclusion to be deduced from this observation formed the basis of our overarching hypothesis that bacterial killing occurs in two stages: ROS-induced membrane damage followed by enzymatic bacterial degradation.

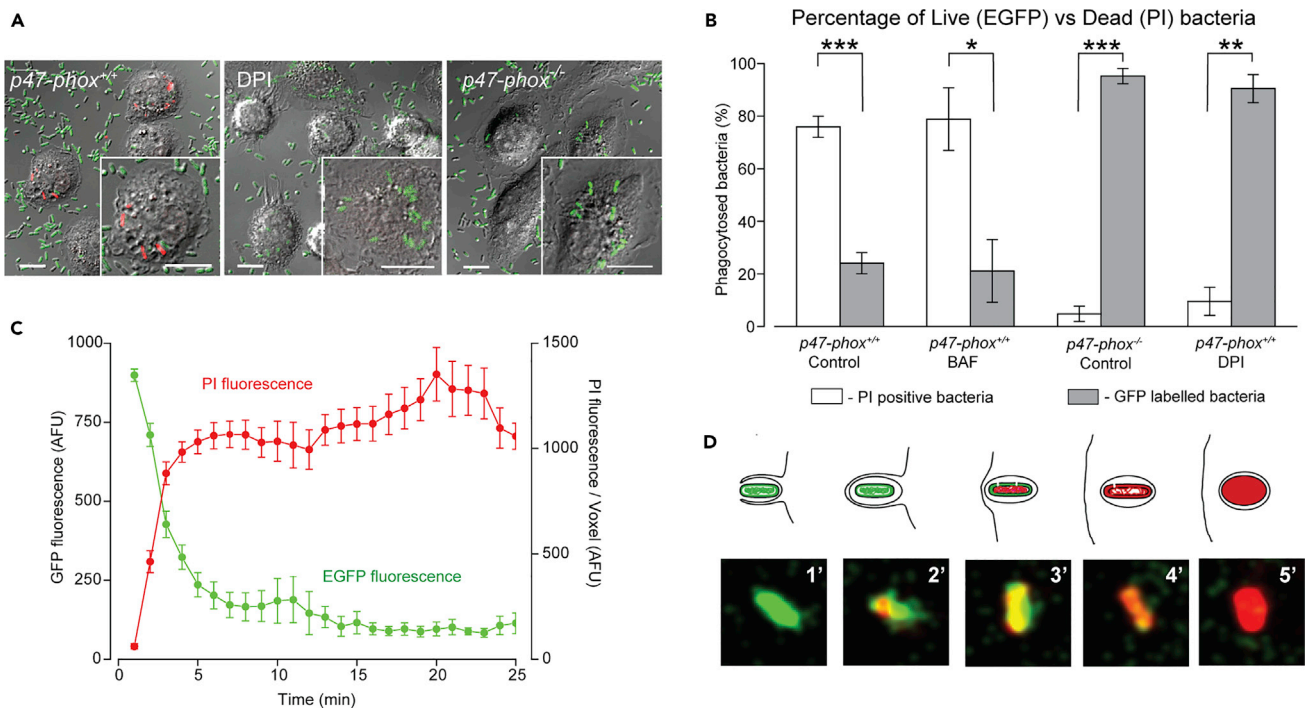

Figure 2. Bacterial Damage Assayed with Propidium Iodide Incorporation

(A) Representative composite images (gray, DIC; red, PI; green, EGFP) of AMs obtained at 30 min after adding EGFP bacteria in *p47-phox*$^{+/+}$ Control; in the presence of 10 μM DPI, and in *p47-phox*$^{-/-}$ (scale bar, 10 μm).

(B) Comparative percentage of "Live" (EGFP positive) versus "Dead" (PI positive) phagocytosed bacterial distribution in *p47-phox*$^{+/+}$ Control (n = 114 cells, 378 bacteria); *p47-phox*$^{+/+}$ + 1 μM BAF (n = 70 cells, 320 bacteria); *p47-phox*$^{+/+}$ + 10 μM DPI (n = 86 cells, 562 bacteria); in *p47-phox*$^{-/-}$ Control (n = 34 cells, 169 bacteria). Significance levels: *p < 0.05, **p < 0.001, ***p < 0.0001 (one-way ANOVA).

(C) Averaged time course of bacterial GFP fluorescence change (green trace, n = 59 bacteria) and associated PI fluorescence change (red trace, n = 59 bacteria) during phagocytosis.

(D) Schematic presentation (above) and representative images (below) of a time course of PI (red) incorporation into an EGFP (green)-labeled bacterium during phagocytosis.

During the experiments carried out on *p47-phox*$^{-/-}$ cells, we noticed large crystalline formations within the mutant cells (see Figure S2), which concerned us that these observable cytoplasmic inclusions might have an effect on cellular function. Observations to this end did not reveal any apparent effect on phagocytic bacterial uptake or on rodent behavior or life span. Similar crystals have been observed previously in neutrophils from *p47-phox*$^{-/-}$-deficient mice and attributed to the protein Ym1 crystallization (Harbord et al., 2002) and associated with eosinophilic crystalline pneumonia (Hoenerhoff et al., 2006) (Liu et al., 2009).

Separation of Oxidative versus Non-oxidative Metabolism in Single Phagosomes Using Fluorescently Labeled Cargo

Dissection of the dual catabolic process, oxidative versus non-oxidative induced bacterial degradation and eventual killing, was approached using two pH-sensitive fluorescent probes, SNARF-1 and pHrodo, conjugated to inert phagocytosed cargo that reported changes in non-overlapping basic and acidic pH ranges, respectively. The probes served as reporters of the kinetics of the multiplexed killing mechanism detecting long recognized pH changes in the phagosome interior following cargo uptake (Segal et al., 1981) (Jankowski and Grinstein, 2002; Jankowski et al., 2002) (El Chemaly et al., 2014) (Levine et al., 2015) (Canton et al., 2014) (Foote et al., 2019). The continued generation of O_2^- anion following NOX activation generated a transient voltage change across the phagosomal membrane owing to anion charge movement into the phagosomal lumen. This voltage gradient eventually drives proton influx through the plasma membrane-derived ion channel Hv1. We detected and tracked the voltage change with second-harmonic generation (SHG) imaging (Figure S3, Video S2). O_2^- generation obligates charge compensation in the low-volume compartment of the phagosome, which is provided by proton influx through Hv1 (Murphy and

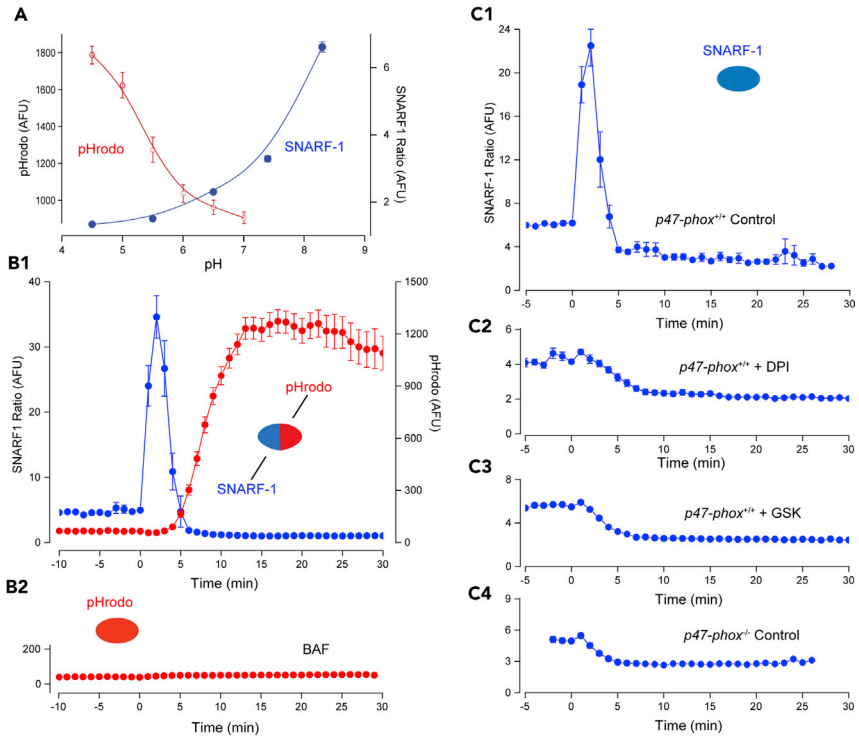

Figure 3. Kinetics of the Two Phagosomal Metabolic Pathways Measured with Fluorochrome Conjugated Zymosan Particles

(A) pH-dependent fluorescence changes for two dyes differing in pKa: pHrodo Green (red empty circles) with pKa approximately 6.5 and SNARF-1 (blue filled circles) with pKa approximately 7.5.

(B1) Time course of intraphagosomal pH changes, measured with zymosan particles doubly conjugated with pHrodo Green (red symbols, n = 34 particles, 12 cells) and SNARF-1 (blue symbols, n = 18 particles, 12 cells).

(B2) Elimination of intraphagosomal acidification, measured with pHrodo Green (red circles, n = 54 particles, 42 cells), after inhibition of V-ATPase by 1 μM BAF.

(C1–C4) Time course of pH changes measured with SNARF-1 labeled zymosan (n = 60 particles, 48 cells) in C1 *p47-phox*$^{+/+}$ Control phagosomes; C2 *p47-phox*$^{+/+}$ in the presence of 10 μM DPI (n = 18 particles, 11 cells); C3 *p47-phox*$^{+/+}$ in the presence of 10 μM GSK (n = 51 particles, 46 cells); and C4 in *p47-phox*$^{-/-}$ Control (n = 27 particles, 15 cells).

DeCoursey, 2006) and is associated with a transient alkaline pH change. We captured the NOX activity associated alkaline pH transient using the pH sensor, SNARF-1 (pKa approximately 7.5) (see Figure 3A).

The pH-sensitive probes, pHrodo Red or pHrodo Green (pKa approximately 6.8), were used to assay phagosomal acidification accompanying lysosomal fusion, transfer of acid-activated catabolic enzymes, and subsequent enzymatic bacterial degradation (Figure 3A). Experiments were carried out using doubly conjugated zymosan particles that allowed imaging over the broad pH range in live cell experiments (Figure 3B1).

Following cargo uptake, we observed that the phagosomal lumen undergoes immediate and transient spike of alkalization, during the first 5 min (Figure 3B1). This alkaline transient detected by SNARF-1, which senses pH in the range of 7–8.5, is presumably due to the scavenging of protons by O_2^- released following NOX activation, and is not detected by pHrodo, which senses pH in the range of 4–7. Termination of the alkaline transient appears to be brought about by the influx of protons through the proton channel, Hv1, and can be prolonged by channel inhibition with Zn^{2+} (Figure S4). The use of doubly conjugated zymosan particles indicated a sustained phagosomal acidification, beginning at about 5 min following phagosomal closure (synchronized with the initiation of the alkaline transient). The V-ATPase inhibitor, bafilomycin (BAF, 1μM), fully inhibited the acidification response (Figure 3B2). The alkalinization response (Figure 3C1) was blocked by the inhibitors of NOX signaling, DPI (10 μM) and GSK2795039 (GSK, 10 μM), and was absent in AMs isolated from *p47-phox*$^{-/-}$ mice lacking NOX activity (Figures 3C2–3C4) supporting the link to O_2^- generation.

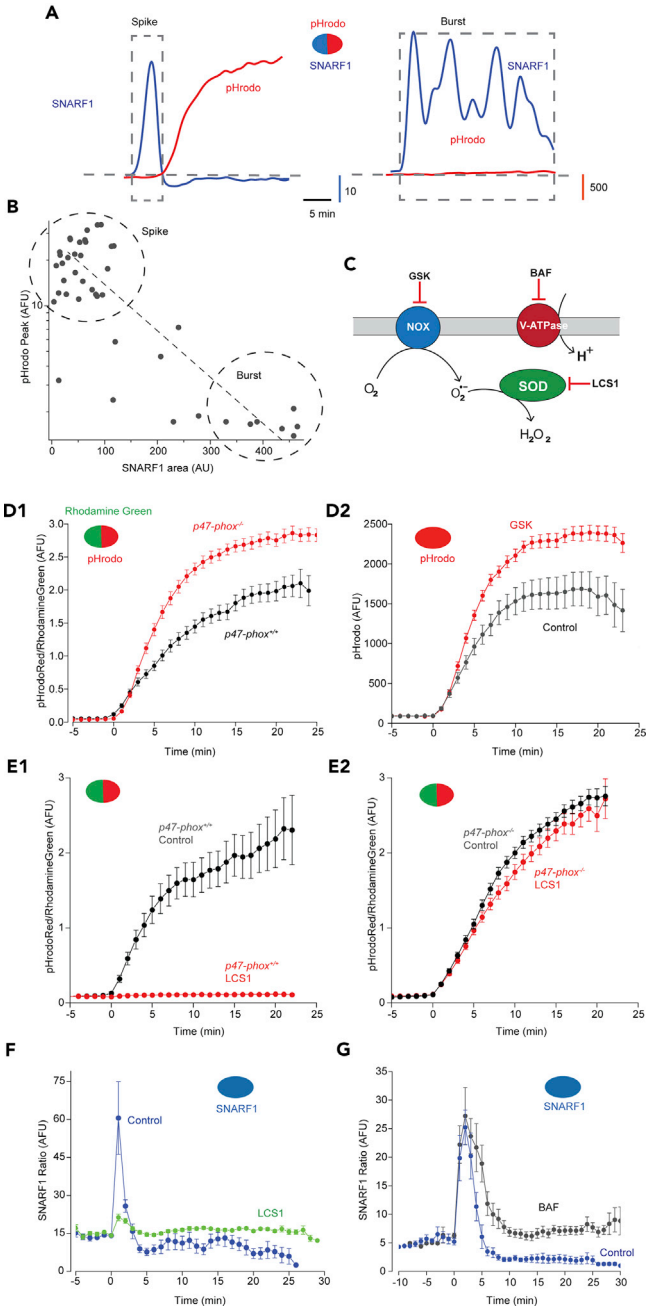

Figure 4. Interaction between Oxidative Response and V-ATPase-Induced Acidification

(A) Two representative types of oxidative responses in phagosomes: a short spike with variable amplitudes (Spike) and prolonged spiking (Burst) were measured by changes in SNARF-1 signal (blue traces), using doubly labeled zymosan particles, as in Figure 2B1; simultaneous changes in acidification were recorded by changes in pHrodo signal (red traces).

(B) Plot of pHrodo peak signal at 30 min versus associated SNARF-1 signal changes integrated as a function of time for a time window when the signal was above its initial baseline level, and fitted by linear regression. (n = 44 phagosomes, n = 15 cells).

(C) Schematic illustration of the pathways affected by pharmacological inhibitors, allowing for the separation of the two catabolic pathways.

(D1) Phagosomal acidification in AMs from *p47-phox*$^{+/+}$ (black trace, n = 51 particles, 18 cells) and *p47-phox*$^{-/-}$ (red trace, n = 55 particles, 26 cells), measured with doubly labeled zymosan particles (pHrodo Red and Rhodamine Green). In this set of experiments, pHrodo Red was used as the pH sensor and Rhodamine Green as the content marker.

Figure 4. *Continued*

(D2). Phagosomal acidification measured with pHrodo Red labeled zymosan in *p47-phox*$^{+/+}$ Control AMs (black trace, n = 50 particles, 49 cells) and in the presence of the NOX inhibitor GSK (red trace, 10 μM, n = 96 particles, 79 cells).

(E1) Phagosomal acidification measured with pHrodo Red and Rhodamine Green labeled zymosan in *p47-phox*$^{+/+}$ AMs in the absence (Control, black trace, n = 26 particles, 12 cells) and in the presence of the SOD inhibitor, 10 μM LCS1 (LCS1, red trace, n = 52 particles, 24 cells).

(E2) Phagosomal acidification measured with pHrodo Red and Rhodamine Green labeled zymosan in *p47-phox* $^{-/-}$ AMs in the absence (Control, black trace, n = 59 particles, 20 cells) and in the presence of 10 μM LCS1 (LCS1, red trace, n = 84 particles, 28 cells).

(F) Oxidative spikes in *p47-phox*$^{+/+}$ AMs measured with SNARF-1 in the presence (LCS1, green trace, n = 62 particles, 38 cells) and absence (Control, navy trace, n = 10 particles, 9 cells) of the SOD inhibitor, 10 μM LCS1. Inhibition of SOD significantly decreased alkaline spike amplitude.

(G) Similar SNARF-1 spike measurements done in *p47-phox*$^{+/+}$ cells in the presence of the V-ATPase inhibitor 1 μM BAF (BAF, black trace, n = 17 particles, 15 cells) or in its absence (Control, navy trace, n = 21 particles, 19 cells) did not abolish the transient time course of SNARF-1 indicating that the decline in phagosomal alkalization was not due to the onset of v-ATPase induced acidification.

NOX Pathway Activation Provides Negative Feedback Regulation of Non-oxidative Metabolism, Leading to Phagosomal Heterogeneity

The non-oxidative pathway has been studied extensively in macrophages (Hackam et al., 1997) (Steinberg et al., 2007) (Sun-Wada et al., 2009) (Ip et al., 2010). It is associated with the development of phagosomal acidification, which is Cl^- dependent, and not driven by Hv1 channel-mediated proton influx, as in the NOX oxidative burst, but rather by active proton transport via V-ATPase activity contributed by phagosomal-lysosomal fusion. Charge neutralization is provided by a channel-mediated Cl^- influx. The next set of experiments, involving zymosan particles coupled to the two pH sensors to report the sequential phagosomal changes over a broad pH range, provided evidence for the interaction of the two pathways.

The data, in Figure 4A, demonstrate the variability in alkalization and acidification time courses that we observed between different phagosomes, often between phagosomes within the same cell. By far, the most common response was a sequential change in pH with acidification following the alkalotic transient ("Spike") after approximately 5 min. However, a substantial number of phagosomes failed to show a delayed acidification with the alkalotic SNARF-1 signal characterized by an extended oscillation ("Burst"). This bimodal behavior suggested a regulatory interaction between the two pathways. We quantified our observation by examining the relationship between the amplitude of the pHrodo peak that reports acidification levels and the area underneath the SNARF-1 curve that reports the magnitude of the alkalinizing response. As seen in Figure 4B, the time course and magnitude of the oxidative burst was inversely proportional to the magnitude of the acidification response. When we compared the magnitude of the peak acidification response in phagosomes from *p47-phox*$^{+/+}$ (WT) mice with those from *p47-phox*$^{-/-}$ mice lacking NOX activity, the acidification magnitude was approximately 1.5-fold higher in the NOX-deficient mice (Figure 4D1). The results were identical in cells treated with the NOX inhibitor, GSK (10 μM, Figure 4D2). After treatment of cells with the superoxide dismutase (SOD) inhibitor, LCS1 (10 μM), which prevents the conversion of O_2^- to hydrogen peroxide (H_2O_2) thus sustaining elevated levels of phagosomal O_2^-, we observed an abrogated acidification response suggesting that the elevation of O_2^- plays a role as regulatory mediator of phagosomal acidification (Figure 4E1). The LCS1- induced decrease in acidification was absent in the *p47-phox*$^{-/-}$ cells (Figure 4E2). Elimination of the SNARF-1 transient, in the presence of the SOD inhibitor LCS1 (10 μM, Figure 4F), further supports the hypothesis that O_2^- dismutation into H_2O_2 during the transient alkalization is due to H^+ scavenging. Inhibition of the non-oxidative pathway by BAF (1 μM) (Figure 4G) left the time course and amplitude of the alkaline transient relatively unchanged as compared with the control. Figure 4C schematically illustrates the pharmacological separation of the two catabolic pathways.

Lack of Heterogeneity in Phagosomal Acidification in Cells that Lack NOX Activity

We observed heterogeneity between phagosomes in single cells, not only with respect to NOX activity, as assayed by alkalotic transient time course summarized in Figure 4, but also with respect to phagosomal acidification, as seen in Figure 5. To demonstrate this phenomenon, zymosan particles doubly conjugated with pH-insensitive Rhodamine Green as a content marker and pHrodo Red as the pH sensor were used to follow the time course and presence of phagosomal acidification. Under control conditions

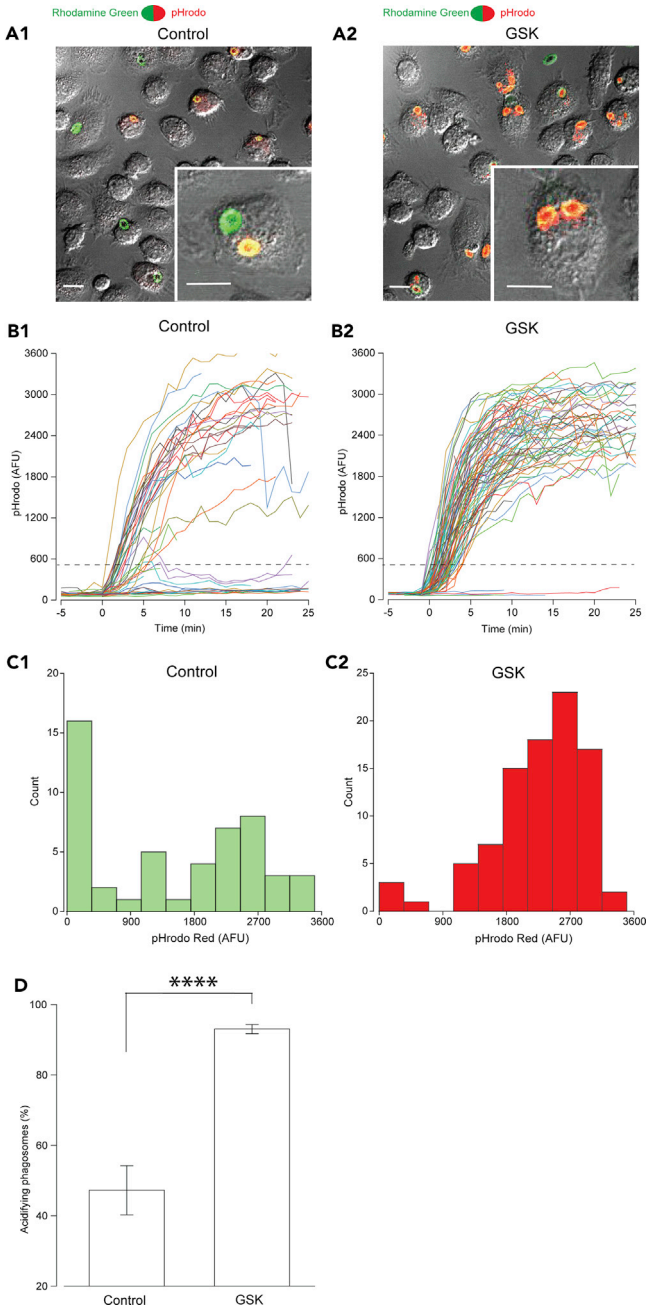

Figure 5. Phagosomal Acidification Heterogeneity in *p47-pho*$^{+/+}$ is ROS Dependent

(A1 and A2). Representative images of relative phagosomal acidification levels at 30 min after addition of doubly labeled zymosan (pHrodo Red and Rhodamine Green) in two conditions: Control (A1) or in the presence of 10 μM GSK (A2) to inhibit NOX activity (scale bar, 10 μm).

(B1 and B2). Time dependence of pHrodo Red fluorescence intensity changes in phagosomes from Control AMs (B1) and AMs treated with 10 μM GSK (B2), in a single field of view over a period of 25 min. Dotted line indicates the arbitrary cutoff amplitude threshold used for determining "acidifying" and "non-acidifying" traces.

(C1 and C2). Peak acidification response measured with doubly labeled pHrodo Red and Rhodamine Green zymosan in: Control (C1, green bars) and 10 μM GSK (C2, red bars) treated cells from acidification traces in B1 and B2.

(D) Summary plot of "acidifying" and "non-acidifying" phagosomes percentage in two conditions: Control (n = 114 particles, 112 cells) and 10 μM GSK (n = 177 particles, 162 cells). Significance level ****$p < 0.0001$ (one-way ANOVA).

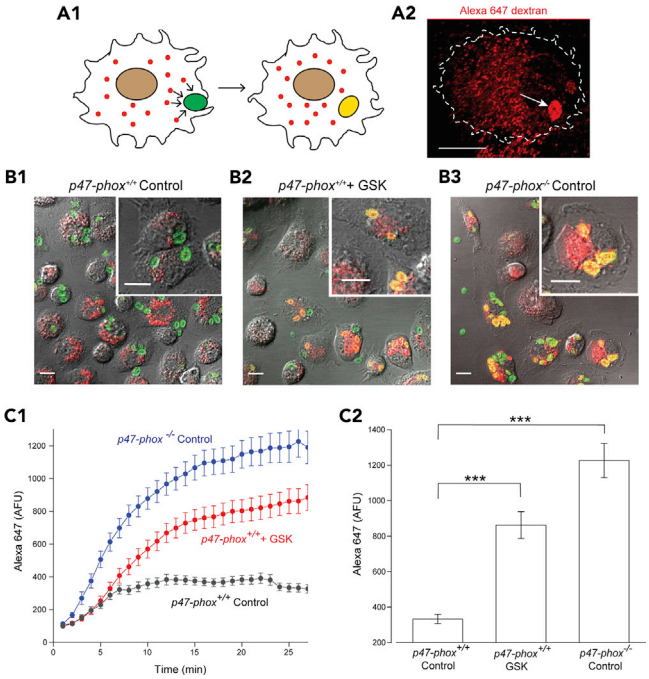

Figure 6. Phagosomal ROS Production Inhibits Phago-Lysosomal Fusion

(A1). Cartoon depicting the phago-lysosomal fusion assay. On the left, AMs preloaded with a pulse of 10,000 MW dextran conjugated with Alexa Fluor 647 for 1 h and were chased for at least 2 h to ensure that endocytosed dextran ended up in lysosomes, thus labeling them red. AMs were then exposed to zymosan particles, conjugated with Rhodamine Green to label phagosome content (green). The fusion of lysosomes with a phagosome is visualized as an increase in the Alexa 647 signal inside the phagosomal compartment, resulting in signal co-localization of Alexa 647 and Rhodamine Green (yellow).

(A2) A confocal microscopy image of a representative AM cell loaded with Alexa 647-dextran, after a 30 min exposure to zymosan particles. The smaller Alexa 647-positive areas indicate lysosomes, whereas an arrow indicates a phagosome filled with Alexa 647 signal contributed by fused lysosomes.

(B1–B3) Composite DIC images (gray) of alveolar macrophages, with Rhodamine Green-labeled phagosomes (green), and Alexa 647-labeled lysosomes (red), after 30 min of zymosan uptake, resulting in the development of yellow colored phagosomes. Comparative acquisition of lysosomal contents by phagosomes, under three different conditions: (B1) *p47-phox*$^{+/+}$ Control AMs, left panel; (B2) *p47-phox*$^{+/+}$ AMs treated with 10 μM GSK (middle panel); and (B3). *p47phox*$^{-/-}$ Control AMs (right panel). Scale bar indicates 10 μm.

(C1 and C2) The rate and magnitude of phago-lysosomal fusion was monitored and visualized by an increase in Alexa 647 signal inside phagosomes. (C1) Comparative kinetics of Alexa 647 dextran incorporation into phagosomes of *p47phox*$^{+/+}$ (black symbols, n = 75 phagosomes from 61 cells); *p47-phox*$^{+/+}$ plus 10 μM GSK (red symbols, n = 55 phagosomes from 52 cells); *p47-phox*$^{-/-}$ (blue symbols, n = 62 phagosomes from 58 cells). (C2) Summary data of relative Alexa 647 dextran incorporation levels in phagosomes at 25 min after adding zymosan in Control *p47-phox*$^{+/+}$ (n = 71 phagosomes, 61 cells); *p47-phox*$^{+/+}$ plus 10 μM GSK (n = 47 phagosomes, 40 cells); Control *p47-phox*$^{-/-}$ (n = 47 phagosomes, 42 cells). Significance level ***$p < 0.001$ (one-way ANOVA).

(Figure 5A1), we observed heterogeneity of acidification levels within AM cells but inhibition of NOX activity with GSK (Figure 5A2) led to a substantial shift in the number of acidifying vesicles. The shift in acidifying vesicles per cell, in the presence and absence of NOX activity, is graphically represented in Figures 5B1 and 5B2. The distribution profile of phagosomal acidification time course, determined from images such as in Figures 5A and 5B, were superimposed, and the peak amplitude at 30 min was compared under conditions of control or NOX inhibition (Figures 5C1 and 5C2). The percentage of acidifying phagosomes (above a defined threshold of 500 AFU) increased from 47.2% in control to 93.0% in the presence of GSK (Figure 5D). These data suggested that a ROS-generated decrease in phagosomal acidification could be due to either a direct regulatory effect on V-ATPase activity (as summarized in Figure 5) or an inhibition of lysosomal fusion, thus preventing the acquisition of the proton pump in the maturing phagosomal membrane. The following set of experiments were designed to distinguish between these two possibilities.

NOX Activity Prevents Lysosomal-Phagosomal Fusion

The next series of experiments allowed for direct visualization and comparison of the acquisition of lysosomal cargo between AMs from *p47-phox*$^{+/+}$and *p47-phox*$^{-/-}$ mice, as well as *p47-phox*$^{+/+}$ cells treated with GSK. Cellular lysosomes were loaded with Alexa 647-conjugated dextran in pulse-chase experiments, as schematically represented in Figure 6A1. Following a period of lysosomal loading, cells were exposed to Rhodamine Green-conjugated zymosan particles used for phagosomal content tracking. The degree of phagosomal-lysosomal fusion was measured as an increase in the Alexa 647-dextran signal acquisition in the phagosomal compartment. A representative cell image of lysosomal-endosomal distribution, and a phagosome filled with Alexa 647-dextran, is shown in Figure 6A2. Phagosomal filling with Alexa 647-dextran, a readout of lysosomal fusion, was significantly increased in cells treated with pharmacological NOX inhibitor, GSK, and in p47-*phox*$^{-/-}$ cells lacking NOX function (Figures 6B1–6B3). This observation was quantitatively examined, following the time course of the increase in Alexa 647 signal, in all zymosan-containing phagosomes (Figure 6C1). Figure 6C2, showing a significant increase in Alexa 647 signal in the absence of NOX oxidase activity, supports the hypothesis that ROS generation, within the phagosome, inhibits subsequent phagosomal-lysosomal fusion and the cascade of catabolic events, which are associated with acidification of phagosomes. However, the experiments do not rule out the possibility that ROS may have an additional direct effect on V-ATPase activity during the initial stages of phagosome formation when lysosomal vesicle contribution to phagosomal membrane area is important to ensure full particle enclosure.

Differential Impact of the Oxidative and Metabolic Pathways on Bacterial Killing in the Phagosome

Final experiments were designed to address a question of how the two separable but interactive pathways, oxidative and metabolic, impact bacterial viability inside the phagosome. To approach this query, we examined the contents of the phagosome at high resolution during the phagocytic process. We began by hypothesizing that bacterial killing and degradation can be directly observed by measuring morphological changes occurring to individual phagocytosed bacteria as shown in sequential images of bacterial trafficking in the phagosome in Figure 2D. We quantified the extent of bacterial viability or killing, inside the phagosome, based on bacterial volume changes with time. These volume changes could then be used to identify both growth and final doubling, or terminal degradation and loss of microorganism integrity. The measure of bacterial volume based on 3D rendering of DsRed fluorescence is a new assay that is potentially widely applicable to measurements of changes in subcellular particles in general. The validity of the methodology is demonstrated in Figures 7A and 7B. DsRed *P. aeruginosa* captured in phagosomes are tracked over time and rendered for volume measurements. Images in Figure 7A are from a bacterium in a phagosome from a p47-phox$^{+/+}$ control cell (Figure 7A1) and a cell that was treated with the NOX inhibitor GSK (Figure 7A2). The obvious doubling of a bacterium in the control cell could be observed at 5 min and in the GSK-treated cell at 15 min. The volume rendering technique is further illustrated with primary imaging data from bacteria in Figure 7B, using renderings of DsRed-expressing *P. aeruginosa* undergoing volume changes over time while enclosed within a phagosome demonstrating both growth and degradation. Changes in bacterial volume, measured by 3D rendering of DsRed fluorescence collected in confocal stacks, allow for the determination of bacterial growth during its doubling (volume increase), as well as degradation over time (volume decrease). We found that DsRed-labeled *P. aeruginosa* volume does not show significant pH dependence in the pH 4–7 range (Figure S5), indicating that acidification alone does not account for pathogen degradation under *in vitro* control conditions. We then examined and compared changes in bacterial volume over time during phagocytosis, under control conditions (*p47-phox*$^{+/+}$), or with AMs exposed to pharmacological NOX inhibition (GSK), or with macrophages from *p47-phox*$^{-/-}$ mice (Figure 7C). Phagosomes within *p47-phox*$^{+/+}$ cells showed a complete loss of *P. aeruginosa* detectable volume at approximately 15 min following bacterial uptake, whereas phagosomes from cells lacking NOX activity showed no decrement in *P. aeruginosa* volume over the same time period, and in fact, they showed an average increase in volume, indicating growth. Next, we addressed the question of dominance, to learn which catabolic pathway was the determinant factor in bacterial killing. We carried out the same experiments, this time exposing cells to the V-ATPase inhibitor, BAF, thereby preventing lysosomal enzyme activation. Time-dependent changes in volume with V-ATPase inhibition were, on average, more stable, indicative of bacterial stasis. However, it should be noted that, in the presence of BAF, there was a larger spread in bacterial volume change, indicative of a larger heterogeneity in the response. Endpoints from the kinetic experiments are summarized schematically and compared in Figure 7D.

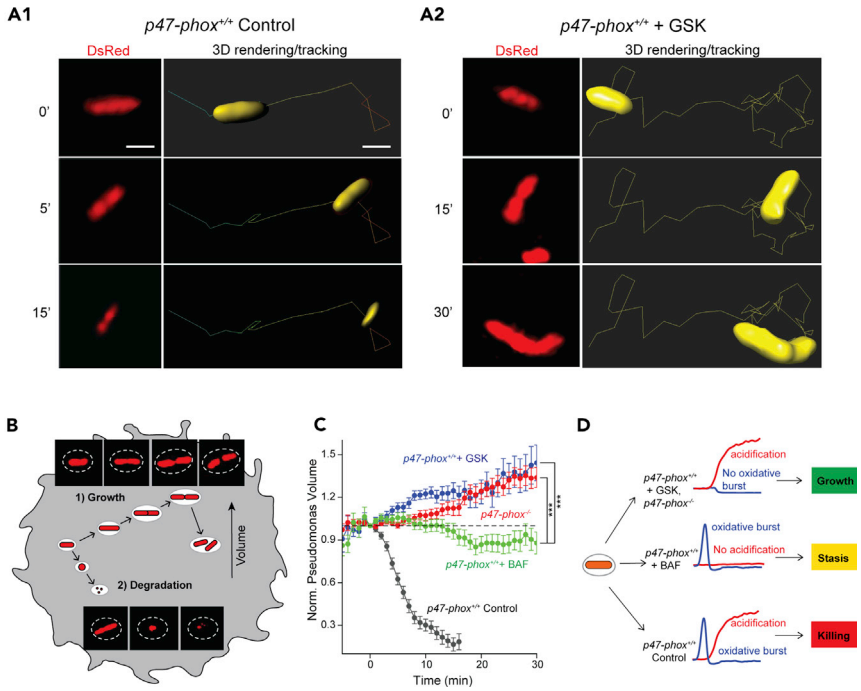

Figure 7. Fast Time Course of Bacterial Degradation Monitored by Bacterial Volume Change

(A1 and A2) Representative deconvoluted images of a phagocytosed DsRed expressing bacterium in fluorescence (red, left panels) and in 3D rendered mode with a tracking trace (yellow) at different indicated times (0–30 min) in *p47-phox*$^{+/+}$ in the absence (A1, *p47-phox*$^{+/+}$ Control) and in the presence of 10 μm GSK (A2, *p47-phox*$^{+/+}$ + GSK) (scale bar, 2 μm).

(B) Schematic representation of bacterial volume changes in phagosomes indicating: (1) bacterial growth; (2) bacterial degradation/killing. Inserts: representative time course images of phagocytosed dsRed expressing *P. aeruginosa* undergoing either bacterial growth (above) or bacterial degradation (below).

(C) Time course of bacterial volume change in: *p47-phox*$^{+/+}$ Control (black trace, n = 57 bacteria from 29 cells); *p47-phox*$^{+/+}$ plus 10 μM GSK (navy trace, n = 34 bacteria from 19 cells); *p47-phox*$^{-/-}$ Control (red trace, n = 35 bacteria from 29 cells); *p47-phox*$^{+/+}$ plus 1 μM BAF (green trace, n = 76 bacteria from 33 cells). Significance level ****$p < 0.001$ (one-way ANOVA).

(D) Schematic diagram summarizing the differential impact of specific catabolic pathway inhibition on phagosomal bacterial survival. (A) Lack of NOX activity induced either by pharmacological inhibition with GSK or by genetic knockout leads to bacterial survival and growth (Growth); inhibition of V-ATPase induced acidification with BAF leads to short-term static survival of bacteria without significant damage or growth (Stasis); intact NOX and V-ATPase functioning leads to rapid bacterial degradation (Killing).

DISCUSSION

We began this study by asking the very basic question, which surprisingly is still open: what process kills a bacterium once it has been phagocytosed by a tissue macrophage? If it is not a single mechanism, we wondered if there is a hierarchy of steps, which, if not carried out in a strict succession, lead to a general static bacterial state in the phagosomal lumen with eventual bacterial escape and cytoplasmic proliferation. It is likely that phagosomal catabolic pathways may well be regulated by specific pathogen secretory products, altering either the magnitude or time course of NOX-dependent O_2^- release or lysosomal enzymatic activity (Podinovskaia and Russell, 2015). In addition, pathogenic antigens may alter the gating of channels or transporters that are integral to the sequential events of O_2^- neutralization or alter anion charge shunt enhancement of V-ATPase activity.

These caveats in mind, we limited our study to a single bacterial species, namely, *P. aeruginosa*, and its interaction with the pulmonary AM. Biological variability, in the answer to our question, will and does involve bacterial secretory products, and defense mechanisms that are unique to the pathogen and the macrophage tissue source, as well as activation state of the cell that has engulfed the microorganism. We chose to study *P. aeruginosa* as it is common in pulmonary disease. Our choice of pathogen also allowed us to examine the phenomenon of bacterial killing using methods well developed in our laboratory

including fluorescent tools and high-resolution live cell microscopic techniques (Di et al., 2006) (Deriy et al., 2009) (Riazanski et al., 2015). The conclusions derived from our study certainly do not generalize to all bacterial species but rather give an insight into the mechanism and intracellular heterogeneity of the phagosomal degradative process in pulmonary tissue macrophages.

In the pulmonary tissue macrophage, absence of either one of the phagosomal catabolic pathways, oxidative or non-oxidative, leads to defective bacterial killing, suggesting a regulatory balance linking this bimodal process. We have characterized the chemical species, namely, O_2^- generated during the oxidative burst, as the element that limits phagosomal acidification through an inhibition of lysosomal fusion, V-ATPase acquisition, and enzymatic pathogen degradation. Our study is the first to resolve the transient time course of the respiratory burst, as separate from sustained acidification, in single phagosomes from pulmonary AMs. Our results are consistent with the hypothesis that, although the phagosomal degradative pathways are separable and interactive in bacterial killing, the oxidative pathway seems to be the *sine qua non*. The relative impact of each of the bactericidal pathways in the context of human disease remains both pathogen and disease dependent, given the spectrum of associated ion transport proteins, channels, or transporters derived from endocytic and plasma membrane sources available to compliment important functions specific either to NOX or acidification activity (see review [Nunes et al., 2013]).

The immunodeficiency in chronic granulomatous disease (CGD), which is the result of genetic defects in any of the five subunits of the NADPH complex, leads to recurring life-threatening infections (Goldblatt and Thrasher, 2000). It has been reported that, in monocytes and macrophages from these patients, the non-oxidative catabolic pathway is still intact but apparently incapable of carrying out pathogen killing efficiently and independently for some bacterial species (Chu et al., 2013). On the other hand, in the disease of cystic fibrosis (CF), the Cl^- channel, Cystic Fibrosis Transmembrane Conductance Regulator (CFTR) that facilitates phagosomal acidification is absent in macrophages in the pulmonary tree and phagosomes are left unable to generate an environment that is optimal for functioning of the catabolic enzymes contributed by lysosomal fusion, thus leaving bacterial killing compromised (Deriy et al., 2009; Di et al., 2006). In the AMs from patients with CF, the oxidative pathway appears intact but insufficient to provide effective pathogen killing (Assani et al., 2017; Cifani et al., 2013). Our data emphasize that both pathways are necessary, but neither one sufficient, to ensure efficient killing of *P. aeruginosa*, or perhaps more broadly, efficient killing of any pathogen (Figure 7). For example, the neutrophil, without the non-oxidative contribution, accomplishes the task of bacterial killing by an elevation in the oxidative burst capacity, but dies following the burst. On the other hand, the degraded pathogen in the pulmonary macrophage serves as a reservoir that can present antigenic peptides to T lymphocytes, thus serving an important role after the final degradation processes.

Our study addressed the question of whether the two catabolic pathways present in the AMs in particular, and tissue macrophages in general, interact with one another in a regulatory loop, or whether their time courses are separable and processes independent. Our data are consistent with a sequential model in which the oxidative pathway results in an initial and transient O_2^- release. As O_2^- is a charged species and does not easily cross cell membranes, it may enter the bacterial periplasm through anion transport proteins or porins (Galdiero et al., 2012) (Benz et al., 1985). In the periplasm, O_2^- is converted to uncharged H_2O_2, thus gaining access to the bacterial cytoplasm where DNA damage and immobilization of pathogen metabolic processes, possibly including toxin or peptide release, can render bacterial death (Slauch, 2011). This process may be reversible depending upon the magnitude of O_2^- release and/or levels of superoxide dismutase (SOD) in the periplasm, but when either element is present at low levels, merely bacterial stasis will occur.

The non-oxidative pathway is dependent not only on the fusion of phagosomes with lysosomes and subsequent injection of enzymatic contents but also on the contribution of the lysosomal V-ATPase. Acidification of the phagosomal compartment by V-ATPase optimizes lysosomal enzymatic activity by contributing the needed protons. This process requires the parallel acquisition of anions, through a Cl^- selective influx pathway, which then serves as charge shunt to the depolarizing effect of an ATP-dependent proton influx. Even though the two pathways, oxidative and non-oxidative, appear to act in a temporal sequence, they are likely to be linked by a reversible change in phagosomal membrane potential, given the complexity of the movement of charged ionic species. Visualization of the time dependence of the voltage change, accompanying phagosomal uptake of bacterium, was identified using the fluorescent technique of second harmonic generation (SHG) and is presented in Figure S2.

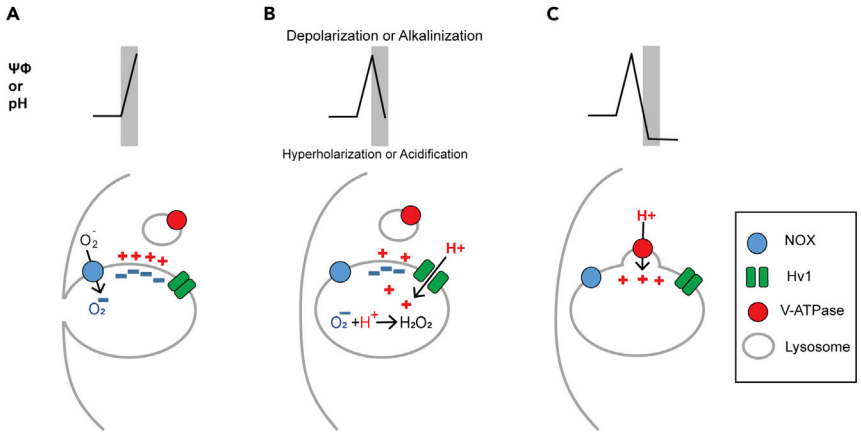

Figure 8. Schematic Overview of Phagosomal Membrane Potential (ΨΦ) and pH Changes during Early Stages of Phagolysosomal Genesis

(A) Electrogenic NOX activity that started prior to phagosomal closure leads to O^-_2 anion flux into the nascent phagosome locally depolarizing the cellular membrane potential, resulting from the associated proton/cation accumulation on the cellular cytoplasmic side. The O^-_2 flux consumes locally available protons, leading to phagosomal alkalinization resultant to proton scavenging during rapid O^{2-} dismutation to H_2O_2. Parallel acidification, which takes place on the cytoplasmic side of the phagosome, inhibits lyso-endosomal fusion to the forming phagosome.

(B) The localized depolarization limits NOX activity and opens voltage-gated Hv1 channels leading to proton influx, which concomitantly neutralizes the cross-phagosomal pH gradient. Consequent phagosomal closure repolarizes phagosomal membrane voltage and closes Hv1 channels.

(C) Mirrored neutralization of the acidic pH on the phagosomal cytoplasmic side permits phago-lysosomal fusion, which contributes V-ATPase proton pumps. V-ATPase activity increases proton influx into the phagosome, producing phagosomal acidification and hyperpolarization obligating Cl^- anion influx as a charge shunt.

Phagosomal function intercalates between two interdependent membrane parameters: pH and membrane voltage. These parameters are both experimentally inaccessible directly, as the phagosome sits in and is dependent upon cellular function. Our analysis of phagosomal function must be deduced indirectly from localized dye experiments analyzed in time as the organelle carries out pathogen destruction. The early initiation of the oxidative burst, which starts before closure of a nascent phagosome, results in release of the anion O^-_2 into the developing phagosomal lumen and induces a local cellular depolarization (Figure 8A). The local cellular depolarization is short lived, accompanied by an alkalotic transient (due to O^-_2 scavenging of protons during its dismutation to H_2O_2), and is terminated by the influx of protons through Hv1 channels. The phagosomal membrane repolarizes upon membrane closure (Figure 8B). The alkalotic transient, absent in *p47-phox*$^{-/-}$ cells (Figure 3C4), is also diminished in the presence of SOD inhibition by LCS1 (Figure 4F). Inhibition of SOD would be expected to enhance the intraphagosomal concentration and reduce the decay of O_2^-. The observed transient intra-phagosomal alkalization associated with anion O^-_2 influx that we observed is likely to be accompanied by cytoplasmic acidification (positive charge build-up) adjacent to a phagosome. In this case, the accumulation of positive charge at the surface of the phagosome would serve to modify the gating of and enhance the driving force through Hv1 channels, thereby facilitating proton influx into the phagosome used to neutralize O^-_2. The hyperpolarization of nascent phagosomes, as schematized in Figures 8A is sensed as a plasma membrane depolarization by voltage-gated channels, including Hv1 (Figure 8B). The buildup of positive charge at the outside of the nascent phagosome following the increase in phagosomal O^-_2 would be seen as a transient cytoplasmic acidification. Such transient increases in cytoplasmic acidification have been observed in phagocytosing neutrophils loaded with membrane permeant SNARF1 and these changes were modulated by Zn^{2+} inhibition of proton Hv1channels (Morgan et al., 2009). Finally, phago-lysosomal fusion that contributes V-ATPase activity, terminates the alkalotic transient giving rise to sustained phagosomal acidification (Figure 8C).

The two catabolic processes appear to be linked further in a second inhibitory feedback interaction: the generation of O_2^- and/or buildup of O_2^- inhibits lysosomal fusion and consequently acid-dependent enzymatic cargo digestion (Figure 3). We have shown and quantified for the first time in single phagosomes that lysosomal fusion and the initiation of macrophage phagosomal acidification is inhibited during prolonged intra-phagosomal alkalinization and subsequent O_2^- buildup (Figures 3A and 3B). In a similar manner,

inhibition of SOD activity, which would be expected to increase O_2^- within the phagosome by blocking H_2O_2 formation, completely inhibited phagosomal acidification (Figure 3D). Our data are consistent with that of Jankowski and colleagues in the neutrophil, showing that acquisition of V-ATPases into the phagosomal membrane is inhibited during oxidase activity (Jankowski et al., 2002).

In our experiments, the primary cultured AMs were not divided into two distinct polarized populations, M1 and M2, differentiated on the basis of their acidification responses to phagocytic cargo. Phagosomal heterogeneity was commonly observable even within a single cell in the absence of differentiation stimuli. Identification of macrophages into these functional phenotypes has become increasingly broad and bipolar (Martinez and Gordon, 2014). Existence of such populations has been described for macrophages derived from *in vitro* GM- or M-CSF differentiated, human peripheral blood mononuclear cells as based on their phagosomal pH regulation (Canton et al., 2014) (Canton, 2014) (Foote et al., 2019). In stark contrast, we observed homogeneity in phagosomal pH responses in cultured AMs only by inhibiting NOX in the entire population. Although in our studies, we did not attempt to experimentally polarize cultured AMs as in previous studies of blood monocytes in culture (Canton et al., 2014) (Foote et al., 2019), the heterogeneity of single cell phagosomal pH would suggest that it is not a good predictor of cellular subtype.

Our studies on the comparative kinetics of the two catabolic pathways in phagosomes *in situ,* were directly translatable into bactericidal impact and predict that treatments affecting the magnitude of NOX expression or its activity might have significant impact on bacterial killing at enhanced bacterial loads. Using a novel, fluorescence microscopy imaging assay, focused on tracing changes in bacterial morphology directly inside the phagosome, we have shown for the first time that the time course of the gram-negative bacterial degradation/killing is rather short and occurs within 15 min. The use of the single, phagosomal bacterial imaging assay eliminates possible errors, due to differences in phagocytic index under different conditions or between different genotypes, and requires a significantly lower number of cells than in classical CFU assays.

In summary, we have explicated the chain of catabolic biochemical reactions triggered upon initiation of phagocytosis and their individual impact eventually leading to killing and decomposition of the ingested pathogens. We have identified and measured simultaneously the relative time course and contribution of the NOX-mediated oxidative burst, as well as metabolic acidification, to the microbicidal effect on *P. aeruginosa*. We have documented bacterial killing in individual phagosomes from murine alveolar macrophages (AMs) that we isolated from either *p47-phox*$^{+/+}$ or *p47-phox*$^{-/-}$ mice. The catabolic processes are sequential and separable, starting with transient NOX activity, which is electrogenic and identifiable as a transient alkalinization that precedes phagosomal acidification. The brief oxidative burst producing an influx O_2^- into the phagosome leads to a phagosomal hyperpolarization favoring the inward movement of protons through the proton channel Hv1 and, ultimately, charge neutralization. The generation of O_2^- is sufficient to permeabilize the entrapped pathogen, thus contributing to the initial impairment, which is followed by further degradative processing through the action of lysosomal enzymes in the acidified environment. Significantly, we did not find alkalinization/acidification variability among cells as would be predicted if this property were to be restricted to M1 and M2 subtypes, but rather we found variability among phagosomes in individual cells. This is indicative of perhaps an uneven distribution of key enzymes and ion channels in the phagosome during uptake of the pathogen as it is enclosed by plasma membrane and associated membrane bound transporters in a random fashion. Unexpectedly, we and others (Canton et al., 2014) have observed that excessive O_2^- generation, detected as extended alkalinization during the initial oxidative burst, prevented subsequent lysosomal fusion and phagosomal V-ATPase acquisition. Thus, the relative magnitude of NOX activity in AMs is the dominant upstream factor in controlling bacterial killing, in general, and *P. aeruginosa* in specific, as shown by our high-resolution *in situ* image-based bacterial killing assay. The absence of NOX activity favors stasis or even growth of bacteria in the phagosomal compartment. Quantitative analysis of the processes that control microbicidal function in the phagosomal compartment will direct future design of directed therapeutic control of severe pulmonary infection. This will require maintaining a delicate therapeutic balance between NOX activity and phagosomal acidification.

Limitations of the Study

We limited our study to a single bacterial species, namely, *P. aeruginosa,* and its interaction with the pulmonary AM. Biological variability, in the answer to our question, will and does involve bacterial secretory products, and defense mechanisms that are unique to the pathogen and the macrophage tissue source, as well as activation state of the cell that has engulfed the microorganism. We chose to study *P. aeruginosa* as it is common in

pulmonary disease. Our choice of pathogen also allowed us to examine the phenomenon of bacterial killing using methods well-developed in our laboratory including fluorescent tools and high-resolution live cell microscopic techniques (Di et al., 2006) (Deriy et al., 2009) (Riazanski et al., 2015). The conclusions derived from our study certainly do not generalize to all bacterial species, but rather give an insight into the mechanism and intracellular heterogeneity of the phagosomal degradative process in pulmonary tissue macrophages.

Resource Availability

Lead Contact

Further information and requests for resources and reagents should be directed to and will be fulfilled by the lead Contact, Deborah J. Nelson (nelson@uchicago.edu).

Materials Availability

This study did not generate new unique reagents.

Data and Code Availability

No unpublished custom code, software, or algorithm was used to support the main claims of the paper.

METHODS

All methods can be found in the accompanying Transparent Methods supplemental file.

SUPPLEMENTAL INFORMATION

Supplemental Information can be found online at https://doi.org/10.1016/j.isci.2020.101759.

ACKNOWLEDGMENTS

The authors want to thank Dr. Ajay Shah of King's College, London who generously offered the use of his LysM-Cre Nox2−/− (p47-phox−/−) mice. The mice were donated by Dr. Lev Becker who originally housed the colony at the University of Chicago. The authors thank the many helpful conversations and editorial time given by Drs. Howard Shuman, Aida Gabdoulkhakova, Radmila S. Stanic, Mary E. Brown, Adriana Zimnicka, and Gerardo Mauleon during the course of the study. Lin S. Boynton designed the proposed cover illustrations. Data in Figure 1C was obtained by Mary E. Brown. This work was supported by NIH RO1 GM36823 (D.J.N.) and NIH RO1 HL25076 (D.J.N.).

AUTHOR CONTRIBUTIONS

Conceptualization, V.R. and D.J.N.; Methodology, V.R. and D.J.N.; Investigation and Writing, V.R., Z.S., and D.J.N.; Funding Acquisition, D.J.N.; Resources, D.J.N; Supervision, V.R. and D.J.N.

DECLARARATION OF INTERESTS

The authors declare no competing interests.

Received: May 15, 2020
Revised: September 7, 2020
Accepted: October 29, 2020
Published: November 20, 2020

REFERENCES

Assani, K., Shrestha, C.L., Robledo-Avila, F., Rajaram, M.V., Partida-Sanchez, S., Schlesinger, L.S., and Kopp, B.T. (2017). Human cystic fibrosis macrophages have defective calcium-dependent protein kinase C activation of the NADPH oxidase, an effect augmented by burkholderia cenocepacia. J. Immunol. *198*, 1985–1994.

Benz, R., Schmid, A., and Hancock, R.E. (1985). Ion selectivity of gram-negative bacterial porins. J. Bacteriol. *162*, 722–727.

Canton, J. (2014). Phagosome maturation in polarized macrophages. J. Leukoc. Biol. *96*, 729–738.

Canton, J., Khezri, R., Glogauer, M., and Grinstein, S. (2014). Contrasting phagosome pH regulation and maturation in human M1 and M2 macrophages. Mol. Biol. Cell *25*, 3330–3341.

Chu, J., Song, H.H., Zarember, K.A., Mills, T.A., and Gallin, J.I. (2013). Persistence of the bacterial pathogen Granulibacter bethesdensis in chronic granulomatous disease monocytes and macrophages lacking a functional NADPH oxidase. J. Immunol. *191*, 3297–3307.

Cifani, N., Pompili, B., Anile, M., Patella, M., Diso, D., Venuta, F., Cimino, G., Quattrucci, S., Di Domenico, E.G., Ascenzioni, F., et al. (2013). Reactive-oxygen-species-mediated *P. aeruginosa* killing is functional in human cystic fibrosis macrophages. PLoS One *8*, e71717.

DeCoursey, T.E. (2016). The intimate and controversial relationship between voltage-gated proton channels and the phagocyte NADPH oxidase. Immunol. Rev. *273*, 194–218.

Deriy, L.V., Gomez, E.A., Zhang, G., Beacham, D.W., Hopson, J.A., Gallan, A.J., Shevchenko, P.D., Bindokas, V.P., and Nelson, D.J. (2009). Disease-causing mutations in the cystic fibrosis transmembrane conductance regulator determine the functional responses of alveolar macrophages. J. Biol. Chem. *284*, 35926–35938.

Di, A., Brown, M.E., Deriy, L.V., Li, C., Szeto, F.L., Chen, Y., Huang, P., Tong, J., Naren, A.P., Bindokas, V., et al. (2006). CFTR regulates phagosome acidification in macrophages and alters bactericidal activity. Nat. Cell Biol. *8*, 933–944.

El Chemaly, A., Nunes, P., Jimaja, W., Castelbou, C., and Demaurex, N. (2014). Hv1 proton channels differentially regulate the pH of neutrophil and macrophage phagosomes by sustaining the production of phagosomal ROS that inhibit the delivery of vacuolar ATPases. J. Leukoc. Biol. *95*, 827–839.

Flannagan, R.S., Jaumouille, V., and Grinstein, S. (2012). The cell biology of phagocytosis. Annu. Rev. Pathol. *7*, 61–98.

Foote, J.R., Patel, A.A., Yona, S., and Segal, A.W. (2019). Variations in the phagosomal environment of human neutrophils and mononuclear phagocyte subsets. Front. Immunol. *10*, 188.

Galdiero, S., Falanga, A., Cantisani, M., Tarallo, R., Della Pepa, M.E., D'Oriano, V., and Galdiero, M. (2012). Microbe-host interactions: structure and role of Gram-negative bacterial porins. Curr. Protein Pept. Sci. *13*, 843–854.

Goldblatt, D., and Thrasher, A.J. (2000). Chronic granulomatous disease. Clin. Exp. Immunol. *122*, 1–9.

Hackam, D.J., Rotstein, O.D., Zhang, W.J., Demaurex, N., Woodside, M., Tsai, O., and Grinstein, S. (1997). Regulation of phagosomal acidification. Differential targeting of Na+/H+ exchangers, Na+/K+-ATPases, and vacuolar-type H+-atpases. J. Biol. Chem. *272*, 29810–29820.

Harbord, M., Novelli, M., Canas, B., Power, D., Davis, C., Godovac-Zimmermann, J., Roes, J., and Segal, A.W. (2002). Ym1 is a neutrophil granule protein that crystallizes in p47phox-deficient mice. J. Biol. Chem. *277*, 5468–5475.

Hoenerhoff, M.J., Starost, M.F., and Ward, J.M. (2006). Eosinophilic crystalline pneumonia as a major cause of death in 129S4/SvJae mice. Vet. Pathol. *43*, 682–688.

Ip, W.K., Sokolovska, A., Charriere, G.M., Boyer, L., Dejardin, S., Cappillino, M.P., Yantosca, L.M., Takahashi, K., Moore, K.J., Lacy-Hulbert, A., et al. (2010). Phagocytosis and phagosome acidification are required for pathogen processing and MyD88-dependent responses to *Staphylococcus aureus*. J. Immunol. *184*, 7071–7081.

Jankowski, A., and Grinstein, S. (2002). Modulation of the cytosolic and phagosomal pH by the NADPH oxidase. Antioxid. Redox Signal. *4*, 61–68.

Jankowski, A., Scott, C.C., and Grinstein, S. (2002). Determinants of the phagosomal pH in neutrophils. J. Biol. Chem. *277*, 6059–6066.

Levine, A.P., Duchen, M.R., de Villiers, S., Rich, P.R., and Segal, A.W. (2015). Alkalinity of neutrophil phagocytic vacuoles is modulated by HVCN1 and has consequences for myeloperoxidase activity. PLoS One *10*, e0125906.

Liu, Q., Cheng, L.I., Yi, L., Zhu, N., Wood, A., Changpriroa, C.M., Ward, J.M., and Jackson, S.H. (2009). p47phox deficiency induces macrophage dysfunction resulting in progressive crystalline macrophage pneumonia. Am. J. Pathol. *174*, 153–163.

Martinez, F.O., and Gordon, S. (2014). The M1 and M2 paradigm of macrophage activation: time for reassessment. F1000prime Rep. *6*, 13.

Morgan, D., Capasso, M., Musset, B., Cherny, V.V., Rios, E., Dyer, M.J., and DeCoursey, T.E. (2009). Voltage-gated proton channels maintain pH in human neutrophils during phagocytosis. Proc. Natl. Acad. Sci. U S A *106*, 18022–18027.

Murphy, R., and DeCoursey, T.E. (2006). Charge compensation during the phagocyte respiratory burst. Biochim. Biophys. Acta *1757*, 996–1011.

Nunes, P., Demaurex, N., and Dinauer, M.C. (2013). Regulation of the NADPH oxidase and associated ion fluxes during phagocytosis. Traffic (Copenhagen, Denmark) *14*, 1118–1131.

Piacenza, L., Trujillo, M., and Radi, R. (2019). Reactive species and pathogen antioxidant networks during phagocytosis. J. Exp. Med. *216*, 501–516.

Podinovskaia, M., and Russell, D.G. (2015). Detection and quantification of microbial manipulation of phagosomal function. Methods Cell Biol. *126*, 305–329.

Riazanski, V., Gabdoulkhakova, A.G., Boynton, L.S., Eguchi, R.R., Deriy, L.V., Hogarth, D.K., Loaec, N., Oumata, N., Galons, H., Brown, M.E., et al. (2015). TRPC6 channel translocation into phagosomal membrane augments phagosomal function. Proc. Natl. Acad. Sci. U S A *112*, E6486–E6495.

Segal, A.W., Geisow, M., Garcia, R., Harper, A., and Miller, R. (1981). The respiratory burst of phagocytic cells is associated with a rise in vacuolar pH. Nature *290*, 406–409.

Slauch, J.M. (2011). How does the oxidative burst of macrophages kill bacteria? Still an open question. Mol. Microbiol. *80*, 580–583.

Steinberg, B.E., Huynh, K.K., and Grinstein, S. (2007). Phagosomal acidification: measurement, manipulation and functional consequences. Biochem. Soc. Trans. *35*, 1083–1087.

Sun-Wada, G.H., Tabata, H., Kawamura, N., Aoyama, M., and Wada, Y. (2009). Direct recruitment of H+-ATPase from lysosomes for phagosomal acidification. J. Cell Sci. *122*, 2504–2513.

iScience, Volume *23*

Supplemental Information

Kinetic Separation of Oxidative and Non-oxidative Metabolism in Single Phagosomes from Alveolar Macrophages: Impact on Bacterial Killing

Vladimir Riazanski, Zihao Sui, and Deborah J. Nelson

Supplemental Information

Kinetic separation of oxidative and non-oxidative metabolism in single phagosomes from alveolar macrophages: Impact on bacterial killing

Vladimir Riazanski, Zihao Sui, and Deborah J. Nelson

Supplemental Figures

Figure S1. Kinetics of PI and EGFP fluorescence changes in EGFP expressing *P. aeruginosa* during phagocytosis, Related to Figure 2.

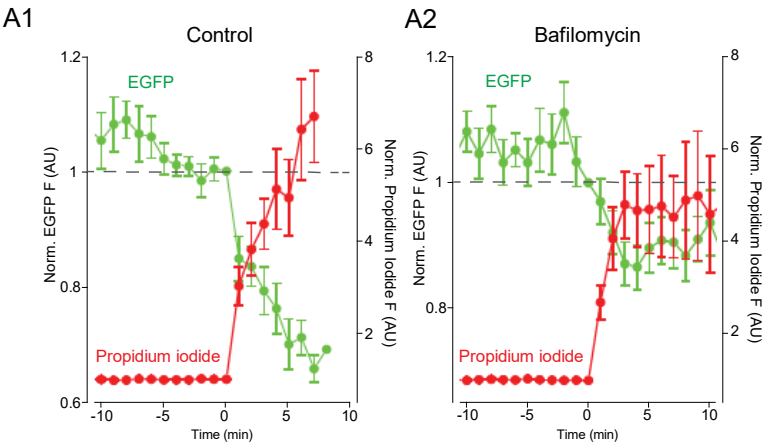

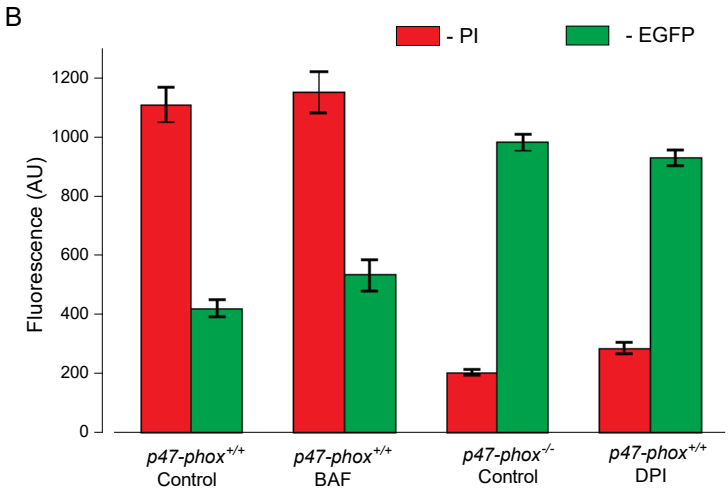

A1. Averaged time course of bacterial EGFP fluorescence change (green trace, n = 16 bacteria) and associated PI fluorescence change (red trace, n = 16 bacteria) during phagocytosis in Control. **A2.** Averaged time course of bacterial EGFP fluorescence change (green trace, n = 23 bacteria) and associated PI fluorescence change (red trace, n = 23 bacteria) during phagocytosis in the presence of 1 μM Bafilomycin. **B.** Comparative PI and EGFP fluorescence mean intensity changes in phagocytosed bacteria: *p47-pho*$^{+/+}$ Control (n=145 bacteria); *p47-pho*$^{+/+}$ + μM BAF (n = 82 bacteria); in *p47-phox*$^{-/-}$ Control (n = 90 bacteria); in *p47-pho*$^{+/+}$ +10 μM DPI (n=107 bacteria).

Figure S2. Large crystalline formations within *p47-phox*$^{-/-}$ macrophages, Related to Figure 2.

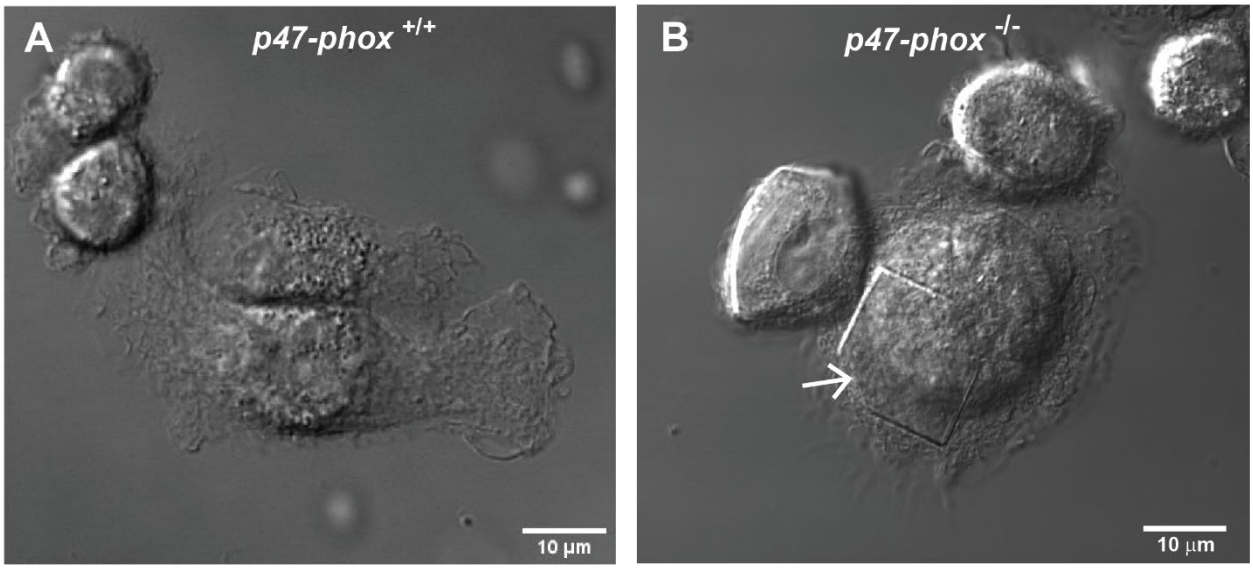

A. Representative live *p47-pho*$^{+/+}$ macrophages visualized with DIC imaging (Scale bar 10 μm).

B. Representative live *p47-pho*$^{-/-}$ macrophages visualized with DIC imaging. An arrow points to a large crystalline structure within a mutant cell (Scale bar 10 μm).

Figure S3. Transient voltage change across phagosomal membrane detected with second-harmonics generation (SHG) imaging, Related to Figure 3.

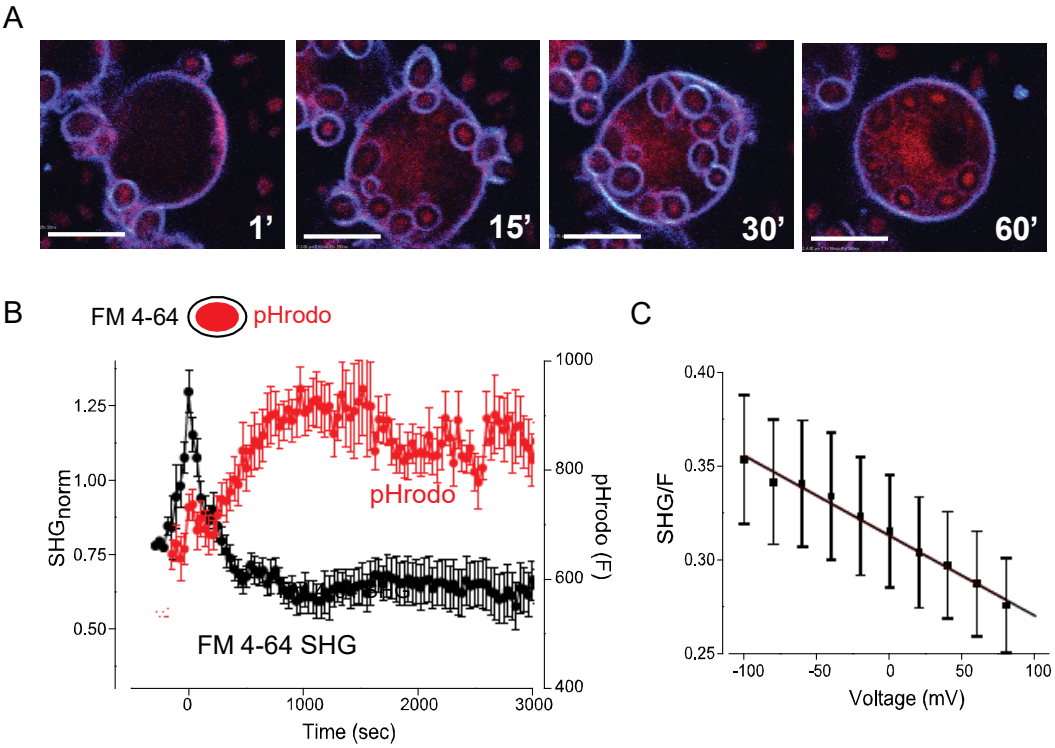

A. Representative composite SHG (blue signal) and pHrodo (red signal) images of J774.1 cells obtained in the presence of 100 μM FM 4-64 at different time points after adding pHrodo Red labelled zymosan (scale bar 10 μm). **B.** Time course of phagosomal pH and SHG changes measured with doubly labelled zymosan: with pHrodo Red (red symbols, n = 13 particles) and FM 4-64 (black symbols, n = 13 particles). **C.** Voltage dependence of FM 4-64 generated SHG/F ratio signal obtained with a combination of whole cell patch-clamp and SHG microscopy (n = 6 cells). Live cell imaging of J774.1 cells exposed to zymosan particles was performed using a 2-photon Olympus CARS imaging system with excitation laser tuned to 900 nm at 3% laser power. Cells were loaded with FM 4-64 (100 μM) for 15 min and incubated for 10 min at 37ºC before imaging. Images were acquired in 1 μm intervals in Z-projections covering whole cell volumes. The SHG emission of FM 4-64 was detected through a band pass filter of 420-460 nm. In **A,** images were acquired following the addition of the zymosan particles. Particle entry into the cells was followed with Imaris software particle tracking algorithm and changes in particle fluorescence

intensity were assayed in 3-D reconstruction plots; particle path length and fluorescent intensity was followed in time.

Figure S4. Changes in alkalization spike kinetics induced by Zinc, Related to Figure 3.

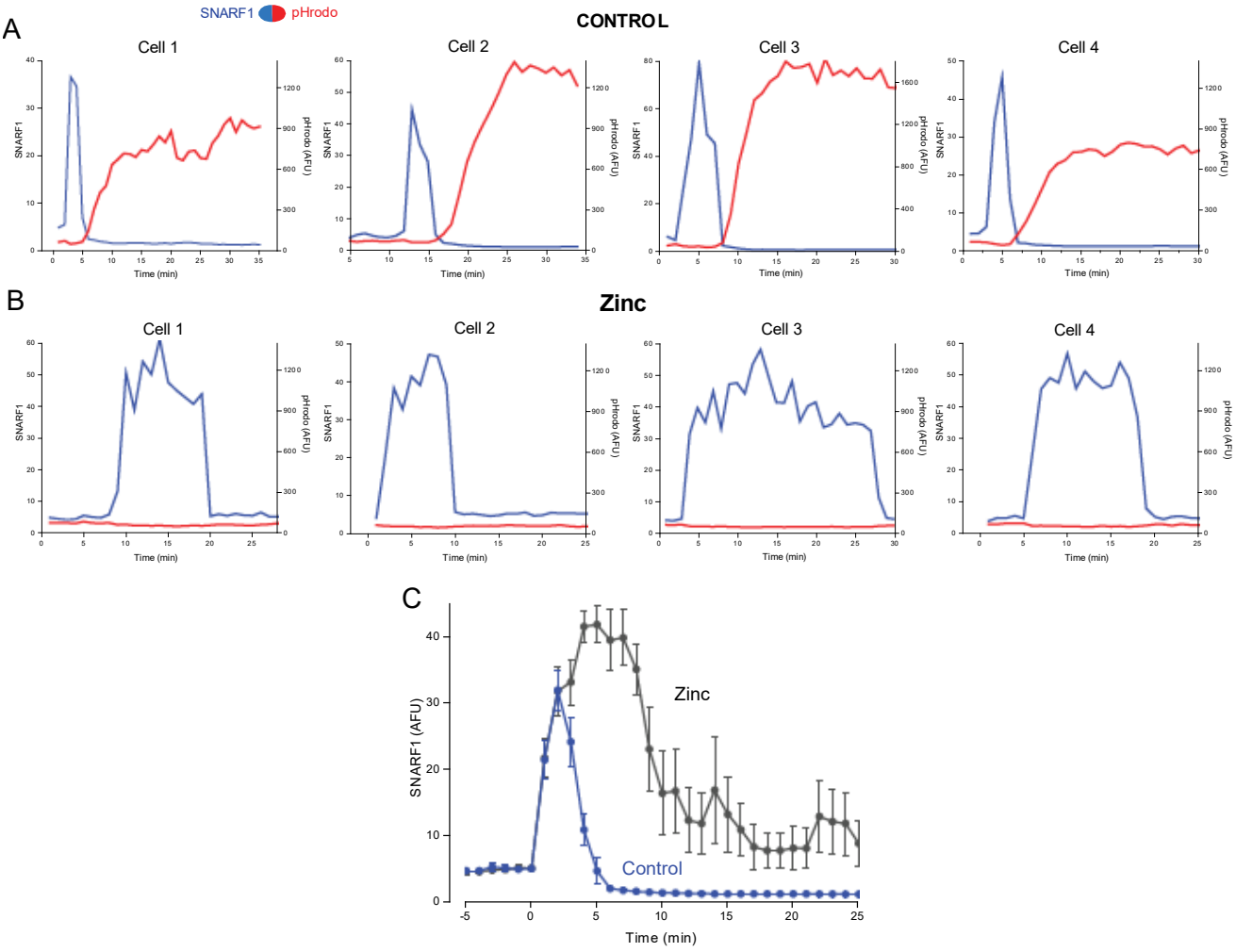

A. Representative kinetics of SNARF-1 (blue traces) and pHrodo (red traces) signal measured with doubly labelled zymosan in Control condition in *p47-pho*$^{+/+}$ AMs. **B.** Representative kinetics of the SNARF-1 (blue traces) and pHrodo (red traces) signal measured with doubly labelled zymosan in presence of 100 μM Zn^{2+} in WT AMs. **C.** Oxidative spikes in *p47-pho*$^{+/+}$ AMs measured with SNARF-1 in the presence (n = 11 particles) and absence (Control, n = 22 particles) of 100 μM Zn^{2+}.

Figure S5. Absence of individual DsRed *P. aeruginosa* volume dependence on extracellular pH, Related to Figure 7.

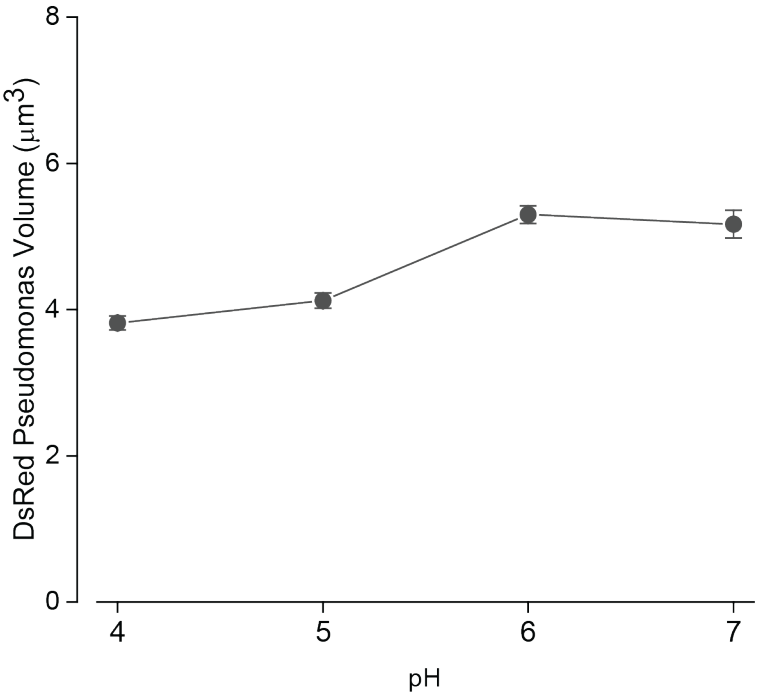

DsRed expressing *P. aeruginosa* were placed in solutions with different pH and confocal fluorescent Z-projections obtained. Phosphate buffered solutions buffered to variable pH with citric acid were used. The Z-stack images were rendered using the surface analysis function of Bitplane Imaris software and volumes of individual bacteria were calculated and averaged (pH 4, n = 378; pH 5, n = 258; pH 6, n = 281; pH 7, n = 140 bacteria).

Transparent Methods

KEY RESOURCES TABLE

REAGENT or RESOURCE	SOURCE	IDENTIFIER
Chemicals, Peptides, and Recombinant Proteins		
Sodium bicarbonate	Sigma-Aldrich	S-5761
Sodium chloride	Sigma-Aldrich	S-9888
D-Sucrose	Fisher Scientific	BP220-212
HEPES	Sigma-Aldrich	H-4034
Potassium chloride	Sigma-Aldrich	P-4504
D-(+)-Glucose	Sigma-Aldrich	G-8270
Difco LB Broth	Becton, Dickinson and Company	244620
Difco Pseudomonas Isolation Agar	Becton, Dickinson and Company	292710
Magnesium chloride hexahydrate	Sigma-Aldrich	M-2393
Calcium chloride	Sigma-Aldrich	C-3881
Zinc chloride	Sigma-Aldrich	Z-4875
DMEM +GlutaMAX -I	Gibco	10569-010
DPBS (1X)	Gibco	14190-144
GSK2795039	MedChemExpress	HY-18950/CS-5988
Bafilomycin A1	Sigma-Aldrich	B1793-10UG
DMSO	Sigma-Aldrich	R10145
pHrodo Red zymosan A BioParticles conjugate	ThermoFisher Scientific	P35364
pHrodo Green zymosan A BioParticles conjugate	ThermoFisher Scientific	P35365
SNARF-1 Carboxylic Acid, Acetate, Succinimidyl Ester	ThermoFisher Scientific	S22801
Alexa 647 dextran (10,000 MW)	ThermoFisher Scientific	D22914
Propidium iodide	ThermoFisher Scientific	P1304MP

FM 4-64	ThermoFisher Scientific	T13320
Zymosan A BioParticles opsonizing reagent	ThermoFisher Scientific	Z2850
Zymosan A	ThermoFisher Scientific	Z2849
Carbodiimide (water soluble) (cyanamide)	Sigma-Aldrich	187364-5G
CellTracker Deep Red Dye	ThermoFisher Scientific	C34565
DPI	Sigma-Aldrich	D-2926
LCS 1	Santa Cruz Biotechnology, Inc	sc-394311
Hygromycin	Sigma-Aldrich	H3274
IPTG	Sigma-Aldrich	I-6758
Gentamicin	Apex BioResearch Products	25-533
Experimental Models: Mice/Organisms/Strains		
C57BL/6 mice	Purchased from Jackson Laboratory and bred in the University of Chicago Animal Resources Center	C57BL/6
LysM-Cre Nox2$^{-/-}$ mice	Obtained from Dr. Ajay Shah, King's College London and bred in the University of Chicago Animal Resources Center	*p47-phox*$^{-/-}$
DsRed expressing *Pseudomonas aeruginosa*	Nelson Lab., The University of Chicago	strain 27853
GFP expressing *Pseudomonas aeruginosa*	Obtained from Dr. Olga Zaborina, The University of Chicago	
Software and Algorithms		
OriginPro	OriginLab Corporation	Version 2019b
ImageJ	NIH	1.53h
Bitplane Imaris software	Andor Technology PLC	version 9.1.2

Huygens Professional for Win64	Scientific Volume Imaging B.V.	18.04. 1p0 64b
Other		
Automated Cell Counter	ThermoFisher Scientific	Countess
35 mm Glass bottom poly-D-lysine coated dishes	MatTek Corporation	P35GC-1.5-10-C
Controlled Enviroment Incubator Shaker	New Brunswick Scientific	
Plate reader	BioTek	Synergy Mx
CO2 incubator	HERAEUS	HERA Cell 150
Osmometer	Advanced Instruments Inc.	Model 3320
pH meter	HORIBA	LAQUA
Leica SP5 Tandem Scanner Spectral 2-photon confocal microscope	Leica Microsystems, Inc.	
Leica TCS SP5 II STED laser scanning confocal microscope	Leica Microsystems, Inc.	

CONTACT FOR REAGENT AND RESOURCE SHARING

Further information and requests for resources and reagents may be directed to and will be fulfilled by the Lead Contact, Deborah J. Nelson (nelson@uchicago.edu).

EXPERIMENTAL DETAILS AND ANIMAL MODEL

Reagents

A list of all reagents used in the study can be found in Key Resources Table. All hydrophobic compounds were dissolved in dimethylsulfoxide (DMSO) as 10 mM stock solutions, while final dilutions into aqueous solutions were made just prior to use. Aliquoted stock solutions were stored at -20°C, thawing only once before use. Care was

taken to use only anhydrous DMSO to avoid compound precipitation upon thawing. To further ensure solubilization of the hydrophobic test compounds, we sonicated the stock solutions for 10-15 min, prior to dilution.

Animals

The studies, detailed herein, conform to the principles set forth by the Animal Welfare Act, and the National Institutes of Health guidelines for the care and use of animals in biomedical research, and were approved by The University of Chicago Institutional Animal Care and Use Committee. All animals were housed in a specific, pathogen-free, biohazard level 2 facility, maintained by The University of Chicago Animal Resources Center (Chicago, IL).

LysM-Cre Nox2$^{-/-}$ (*p47-phox*$^{-/-}$) mice were a kind gift from Dr. Ajay Shah of King's College, London. A colony of the animals is maintained by Dr. Lev Becker at The University of Chicago. Animal genotyping was performed by Transnetyx, Inc., (Cordova, TN).

Bronchoalveolar lavage from mice

Bronchoalveolar lavage (BAL) fluids were collected from mice using standard methods, as previously described (Deriy et al., 2009). The total number of AMs (20-60 μm size) recovered from BAL depended on the genotype and ranged from approximately 0.4-1.2 x 10^4 per mouse. Cells were cultured on Poly-D-lysine coated, glass bottom culture dishes (MatTek Corporation, Ashland, MA) for periods of up to two weeks, in DMEM, 10% FBS, 1% (vol/vol) penicillin-streptomycin, and imaged in HEPES-buffered artificial cerebrospinal fluid (ACSF) solution containing (in mM): 125 NaCl, 2.5 KCl, 10

HEPES, 1.5 $MgCl_2$, 2.5 $CaCl_2$, 10.0 glucose, and 10 Sucrose to adjust osmolarity to 290 mOsm, pH 7.3.

Live cell time-lapse imaging.

Imaging, image processing, and data analysis were performed at the University of Chicago Integrated Light Microscopy Facility. Images were captured with a Leica SP5 Tandem Scanner Spectral 2-photon confocal microscope, and with a Leica TCS SP5 II STED laser scanning confocal microscope (Leica Microsystems, Inc., Buffalo Grove, IL). Image deconvolution, correction of spherical aberration and axial distortion for 3D images were done in Huygens Professional software (Scientific Volume Imaging B.V., Hilversum, Netherlands). Images were filtered and edited using ImageJ software (National Institutes of Health, Bethesda, Maryland, USA). 3D image processing was performed using Bitplane Imaris software v. 9.1.2 (Andor Technology PLC, Belfast, N. Ireland).

Determination of bacterial PI incorporation, phagosomal pH change, phago-lysosomal fusion, and bactericidal activity of AMs.

For bacterial PI incorporation, AMs, isolated from WT and *p47-phox*$^{-/-}$ mutant mice, were cultured on MatTek dishes. At the beginning of experiment, AMs were exposed to GFP-expressing *P. aeruginosa* at 37˚C, in the presence of 60 μM PI in ACSF solution, and imaged every 1 min for 30 min using an inverted, confocal microscope Leica-SP5 with a 63x oil objective.

For the determination of phagosomal pH changes, AMs were exposed to zymosan particles conjugated to a variety of fluorophore combinations, depending upon

experimental goals, and including: SNARF-1; SNARF-1 and pHrodo Green; pHrodo Red; pHrodo Red and Rhodamine Green. SNARF-1 fluorescence was excited with 514 nm laser, and emission collected at two ranges: 560-590 nm and 630-670 nm. Normalized SNARF-1 data were obtained by dividing fluorescent intensity values: 630-670 nm / 560-590 nm. Phagocytosed zymosan particles were imaged every 1 min for up to 1 hour. The fluorescent particles were traced offline, and changes in fluorescence intensities were analyzed using Bitplane Imaris software.

For experiments investigating phago-lysosomal fusion, AMs were exposed to 1 mg/ml Alexa 647 dextran (10,000 MW) in DMEM, 10% FBS at 37°C for 1 hour, then washed several times with DMEM, and incubated additional 2 hours in dextran-free DMEM before imaging. Imaging was done in ACSF solution, following exposure of AMs to Rhodamine Green labelled zymosan, every 1 min for 30 min at 37^0C.

For determination of bactericidal activity, AMs were exposed to DsRed-labeled *P. aeruginosa* at 37^0C, and imaged in live, time-lapse series every 1 min for up to 1 hour, using the inverted confocal microscope Leica-SP5 with a 63X oil objective. The time-lapse images were analyzed offline, and rendered bacterial volumes were obtained using the surface analysis function of Bitplane Imaris software. Bacterial killing, or growth inside AMs, was estimated as DsRed labelled volume change in the sum of Z planes in individual cells over time.

Statistical analysis

To analyze the statistically significant difference between the groups, ANOVA analyses (Student t-test and Mann-Whitney Rank Sum Test) were used. Data are represented as mean ± SEM.